High-velocity impact study of an advanced ceramic using finite element model coupling with a machine learning approach

Alex Yang[a,*], Dan Romanyk[a], James D. Hogan[a]

[a]*Department of Mechanical Engineering, University of Alberta, Edmonton, AB T6G 2R3, Canada*

Abstract

A numerical approach combining finite element modeling and machine learning is used to inform the material performance of an alumina ceramic tile undergoing high-velocity impact. In this study, the alumina ceramic tile is simulated by incorporating a user-defined Johnson-Holmquist-Beissel (JHB) material model within the framework of smoothed particle hydrodynamics (SPH) in LS-DYNA finite element software. The implementation of the JHB model is verified by comparing equivalent stress-pressure responses through a single element simulation test. After implementation, the computational framework is simulated across our chosen range of conditions by matching the results from both plate impact experiments and ballistic testing from the literature. The computational model is then used to generate training data sets for an artificial neural network (ANN) to predict the residual velocity and projectile erosion for an alumina ceramic tile undergoing high-velocity impact in the SPH framework. The ANN is then used to perform a sensitivity analysis involving exploring the effect of mechanical properties (e.g., strength and shear modulus) and impact simulation geometries (e.g., thickness of ceramic tile) on material performance (i.e., residual projectile velocity and erosion). Overall, this study shows the capability of the FEM-ANN approach in studying the high-velocity impact on ceramic tiles and is applicable to guide the structural-scale design of ceramic-based protection systems.

Keywords: High-velocity impact, Ceramic armor, Johnson-Holmquist-Beissel (JHB), Smoothed particle hydrodynamics, Artificial neural network

*Corresponding author

Email address: sy11@ualberta.ca (Alex Yang)

1. Introduction

Advanced ceramics, such as alumina, have been incorporated into the design of various armor systems as frontal layers, mainly owing to their relatively high strength, hardness, and low cost-to-performance ratio [1–3]. To make efforts towards designing and improving armour systems, many experimental and numerical studies have sought to understand the role of mechanical properties and geometries on the dynamic ballistic performance of ceramics [4–7]. Comparing with experimental approaches, numerical approaches enable a wider range of material constants and design parameters to be explored, with improved temporal and spatial resolutions, especially under extreme loading conditions where experimentation and field testing are difficult and costly (e.g., ballistic impact [8], laser shock [9]). For example, ballistic testing in the literature are often conducted within a rather narrow impact velocity range [10], which limits the systematic study of both ballistic (e.g., dwell and penetration [11, 12]) and material responses (e.g., change of mechanisms). Hence, future design strategies and materials development will be largely guided by advancements in numerical approaches after careful verification and validations [13–16], and these will be pursued in this study.

Numerical simulations informed and validated by experiments is a powerful engineering tool for the optimization and design of structures subjected to complex loading conditions (e.g., impact loads [17]). The choices of the material model and the numerical framework plays a key role in the accuracy of predictive results [16]. In the literature, phenomenological models have been extensively implemented to study the behavior of ceramics under the high-velocity impact, such as the Johnson-Holmquist models which considers the strain rate, pressure, bulking, and phase change effects (JH1, JH2, and JHB) [18–20]. A recent study conducted by Islam et al.[21] compared these three models for silicon carbide under ballistic simulations, and it was found that the JHB model resulted in a better prediction of the response of the ceramic than two others (e.g., crack propagation and the cone fracture zone). The improved accuracy by using the JHB model stems from two perspectives: 1. it combines the characteristics of the JH1 and JH2 models in describing material behaviors with consideration of how the material strengths softens from intact state to failed state [20];2. it enables a better characterization on catastrophic failure of ceramics by constituting a piece-wise strength-pressure and damage-pressure envelope leading to a more realistic representation of the response of ceramics subject to impact loading [21, 22]. Accordingly, to better simulate the failure and catastrophic response of ceramics within a computational scheme, this study implements the JHB material model as a user-defined subroutine into the finite element code of LS-DYNA in literature to simulate the response of alumina ceramic tiles under high-velocity impact.

Next, selecting an appropriate physics-based numerical framework is crucial because it can better approximate the system solution and reasonably simulate the crack initiation, propagation, and coalescence in ceramics [16, 23]. Mesh-free methods provide an alternative to the traditional finite element method (FEM) for ballistic impact problems, and theses have been implemented by many researchers in the literature [17, 24, 25]. For example, smoothed particle hydrodynamics (SPH) is suited for large deformation problems as they are able to overcome limitations caused by element distortion existing in FEM due to their mesh-less discretization feature [10, 26, 27]. In conjunction to the proper numerical framework, a comprehensive parametric study and sensitivity analysis of numerical settings in SPH is critical to enhance the simulation accuracy when modelling impacts of brittle solids [28–30]. Large sensitivity of the SPH parameters on impact simulation results have been noted before but not comprehensively studied [21, 28, 31],

such as particle spacing [17], artificial viscosity coefficients [28], and constant applied to smooth length [24]. In this work, parametric studies of these SPH settings are conducted.

In addition, given the considerable computational cost associated with the increasingly sophisticated numerical models and boundary conditions, machine learning (ML) techniques have been employed recently to improve the computational efficiency, and more importantly, enable the possibility of statistical analysis of the behavior of materials across large amounts of input conditions [32, 33]. To the authors' best knowledge, there have been limited impact-related studies to date where artificial computer analysis techniques are used to develop statistical models for describing the performance and properties of materials [34, 35]. Among various techniques (e.g., Bayesian's regression [36] and deep learning [37]), the multilayer perceptron (MLP) approach is the most commonly applied neural network in the field of mechanics [38, 39]. More recently, in the field of impact mechanics, Liu et al. [40] used MLP in combination with a conjugate gradient method to optimize the design of functionally graded metal/ceramic materials. They showed that the neural network possessed good capacity in describing and handling the non-linearity between the design parameters and objective optimization parameter (e.g., depth of penetration) [40]. In a separate study, Bobbili et al. [39] developed a predictive tool based on the MLP method to determine the residual velocity of a projectile impacting an aluminum 1100-H12 thin plate, and they found a good agreement between the experimental and MLP results. Motivated by these limited studies are numerically studying and linking the property and geometrical variables to material performance [39, 40], the present work explores the use of a predictive MLP model coupled with SPH impact simulations to inform the effect of mechanical properties and geometries on impact performance of alumina ceramic tiles, which can then serve as a computationally-efficient tool for material and system design.

In the present study, we first develop a computational framework by combining the user-defined JHB material model and SPH method in LS-DYNA. The computational code was verified through single-element simulation, and the computational framework was simulated by comparing with the experiment's results of plate impacts and ballistic impacts for an alumina ceramic tile [22, 41]. Then, the sensitivity of numerical settings of the SPH method on predicted results (e.g., particle velocity, residual velocity and mass of projectile) are investigated through parametric studies. The results are then used to guide the selection of parameters values for the fully validated and verified models. Lastly, we train an artificial neural network (ANN) with the training datasets obtained from ballistic simulations, which is then applied to study the ballistic performance (e.g., residual projectile velocity) of single alumina ceramic tiles considering both material variation (e.g., strength) and geometry (e.g., tile thickness). The contributions of this work are re-articulated within the following sections: 1. A comprehensive and robust implementation of the JHB material model within the SPH framework in LS-DYNA and the determination of corresponding material constants for alumina are demonstrated (Section 2), followed by verifying the model implementation with a single-element test simulation (see Appendix B). As far as we are aware, this is the first time in the literature where the JHB has been implemented via user subroutine in LS-DYDA. We will make the sub-routine accessible in the supplementary files, thus contributing to future usage [10, 42, 43] and modification in the LS-DYNA solver [10, 17, 44]. 2. Parametric studies on the SPH numerical settings reveal the sensitivities of the settings on key model performance metrics (e.g., residual velocity) (Section 3.1). 3. Structural-scale simulation cases, including plate impact experiments [22] and ballistic testing [41] are conducted

and shown to be in good agreements with the literature (Section 3.2). Finally, an MLP algorithm is then constructed and coupled with the JHB material model to investigate the sensitivity of both material properties and geometries on ballistic performance of alumina tiles undergoing high-velocity impact (Section 4), followed by discussions of the implications for the current study (Section 5).

2. Determinations of material constants

The detailed descriptions of the used Johnson-Holmquist-Beissel (JHB) material model is provided in the Supplementary Material (see Appendix A). Table 1 summarizes all the JHB model parameters for the alumina material used in this work. Specifically, the model constants for alumina are obtained based on the existing experimental data in the literature [45, 46], and calibrated against the shock and ballistic impact validation data (Section 3.2). The initial density, shear modulus, and bulk modulus are obtained from Scazzosi et al. [10], Alexander et al. [45], and Simons et al. [47]. For pressure constants, Alexander et al. [45] examined the dynamic response of alumina under shock loading and generated the test data of pressure vs. relative volume, as shown in Figure 1 (a). The fitted pressure parameters k_1= 265.5 GPa, k_2=181.6 GPa, and k_3= 171.4 GPa are extracted from the fitted curves of the experimental data following the equation noted in the sub-figure and from Equation (8). According to the description in Johnson et al. [20], materials that exhibit phase change shows three distinct response regions under shock loading in their pressure-volume relationship, where the phase transition manifests at a relatively low-pressure state. Figure 1 (a) indicates that the alumina ceramic does not undergo the phase change subjected to high-shocked pressures up to 100 GPa, and as noted by Alexander et al. [45]. As an outcome, the phase change effects are not considered in this work.

For strength constants, Subhash, et al. [46] provided the testing data on a variety of brittle materials that employed a wide range of confinement conditions beyond the HEL (i.e., shock, triaxial compression, and impact experiments). The test data of alumina ceramic are extracted from their work [45] and re-fitted with the constitutive law of the JHB model in Figure 1 (b) using the gradient decent algorithm in Matlab. The values of the intact strength model parameters are determined from the fitted curve: T= 0.20 GPa, σ_i=1.82 GPa, P_i=2.23 GPa, and σ_{max}= 6.83 GPa. The values of the failed strength model parameters are directly extracted from the JH2 curve provided by Bavdekar et al. [46] and then calibrated as: P_f=1.35 GPa, σ_f=1.35 GPa, and σ^f_{max}= 2.7 GPa. The damage constants are provided by Toussaint et al.[17] and then calibrated as D_1=0.03 and n=1. More importantly, to illustrate the improvements in the JHB model, the JH2 intact strength model [18] is also re-plotted in Figure 1 (b). It is observed that the gradually increasing JH2 strength model (i.e., assuming the plot begins at T= 0.20 GPa) deviates from the data points when the stress exceeds the HEL, while the JHB model traces the data points in much better agreement. In summary, the selection of the JHB model describes the three stages of material strength-pressure response with a single curve: 1. linearly at low pressure; 2. non-linearly at higher pressures up to the HEL; and 3. pressure-independent beyond the HEL.

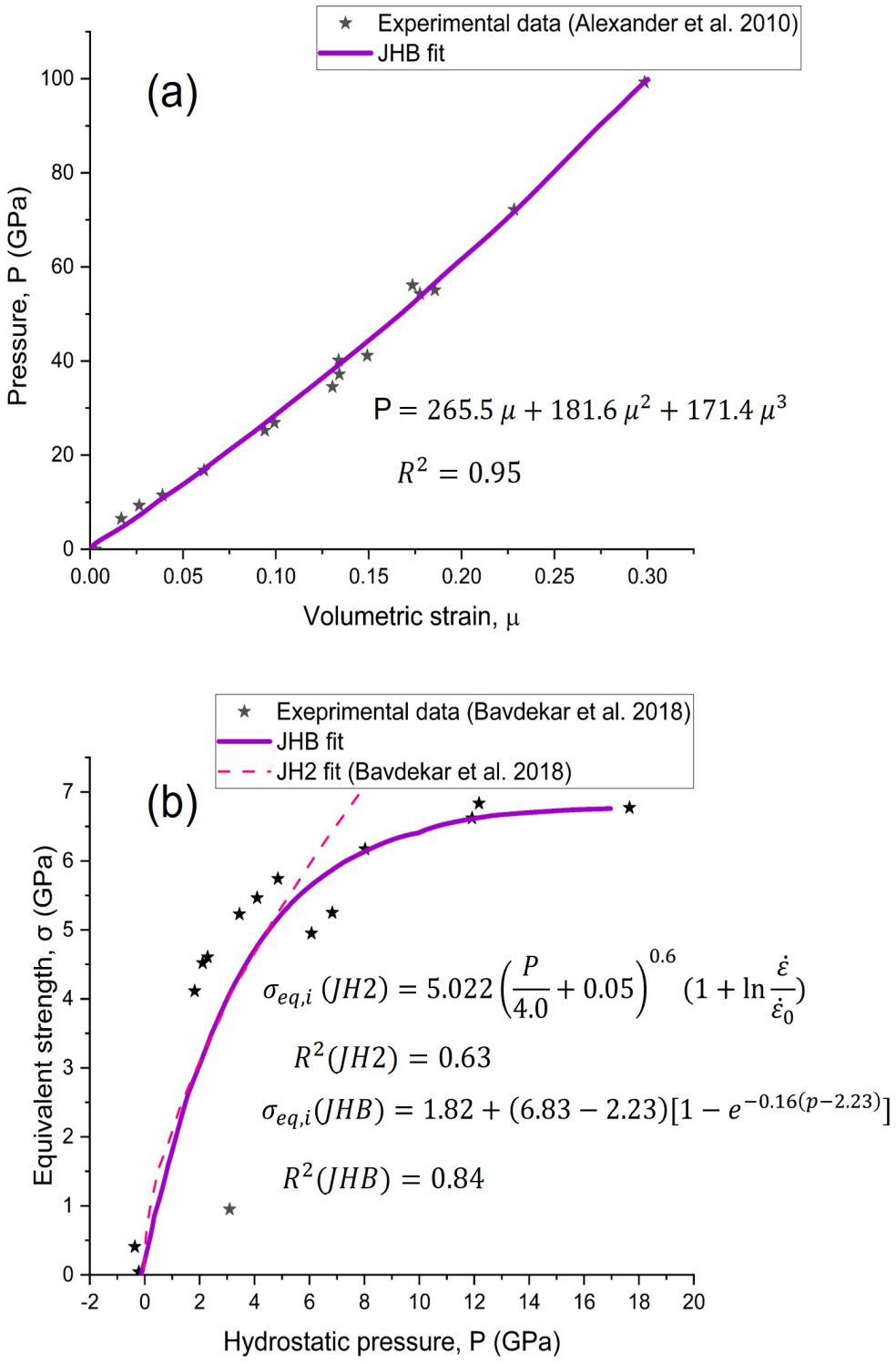

Figure 1: Experimental data from literature [45, 46] with noted curve fits for obtaining the pressure and strength constants of alumina ceramic for the JHB model. (a) Pressure vs. volumetric strain with curve fits for JHB model parametrizations (solid purple) [46], and (b) Equivalent strength vs. hydrostatic pressure with JHB (solid purple) and JH2 (dashed pink) curves fit, demonstrating noted differences between the two models [45].

Table 1: Johnson-Holmquist-Beissel material constants for alumina ceramic.

Model Parameters	Notation	Value
Density (kg/m^3)	ρ	3890 [48]
Shear modulus (GPa)	G	152 [10]
Bulk modulus (GPa)	K	265 [48]
Elastic modulus (GPa)	E	360 [47]
Hydrostatic tensile strength (GPa)	T	0.2 [17]
Intact strength constant (GPa)	σ_i	1.816 [45]
Intact pressure constant (GPa)	P_i	2.228 [45]
Max intact strength	σ_{max}	6.83 [45]
Strain rate coefficient (s^{-1})	C	0.0665 [47]
Failure strength constant (GPa)	σ_f	1.35 [45]
Failure pressure constant (GPa)	P_f	1.35 [45]
Max failure strength	$\sigma^f_{\max}$	2.7 [45]
Reference strain rate (s^{-1})	ϵ_0	1 [49]
Bulking factor	B	1 [49]
Elastic bulk modulus (GPa)	K_1	265 [45]
Coefficient for 2nd degree term in EOS (GPa)	K_2	181.6 [45]
Coefficient for 3rd degree term in EOS (GPa)	K_3	171.4 [45]
Damage coefficient	D_1	0.03 [49]
Damage exponent	n	1 [49]

3. Simulation results and discussions

This section provides the parametric studies on the effects of the numerical settings of SPH within the context of both plate impact (see Figure 2) and ballistic (see Figure 3) testing cases, including the particle spacing, applied constant to smooth length, and artificial viscosity parameters. A better evaluation of these parameters is important given their noted sensitivities in the literature to simulations of various problems [21, 28], and our desire to guide other researchers in the future. The best combinations of SPH parameters for each testing case are identified by matching experimental results in the literature [22, 41], the detailed discussions on a quantitative and qualitative comparison with the experimental data provided in Section 3.2.

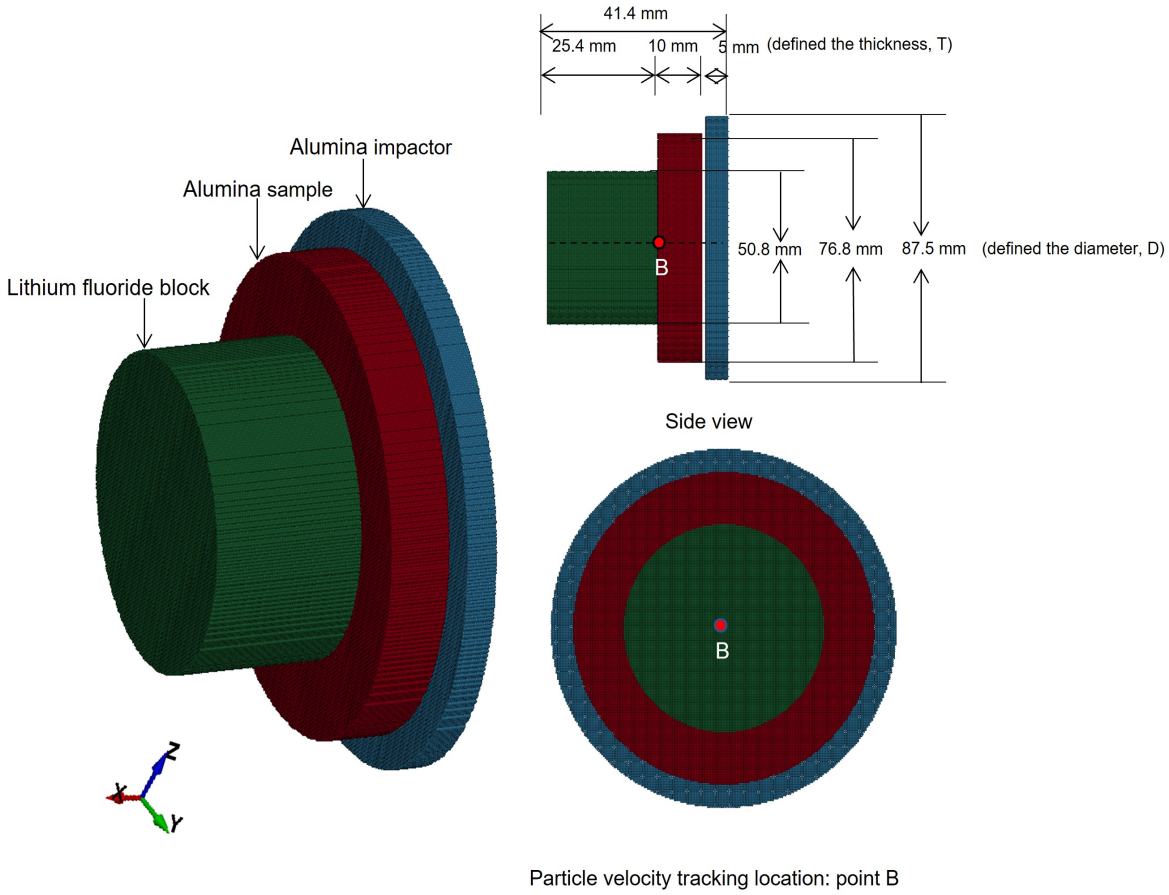

Figure 2: Configuration of the compressive plate impact experiment with an alumina plate impacting on the alumina sample backed by a lithium fluoride block. This configuration is used to conduct parametric studies of SPH numerical settings and parameterize the Johnson-Holmquist-Beissel model by comparing the shock response measured at point B at the center of the back surface of sample. The geometry in this study follows the work by Grady and Moody [22]. Note that the dimensions of the impactor, sample, and block is varied in our simulations based on the ones reported in Grady and Moody [22].

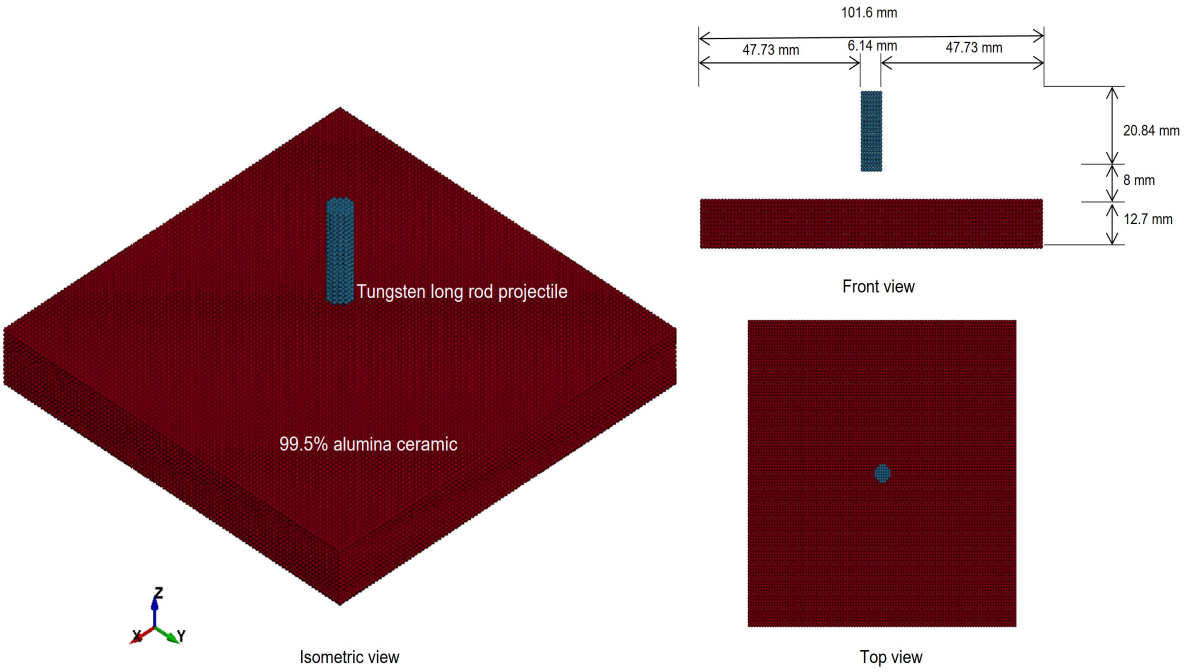

Figure 3: Configuration of the simulation setup of a tungsten long rod impacting on an alumina ceramic tile. The geometries and dimensions of the setup follow the study by Nemat-Nasser et al. [41].

3.1 Parametric studies of the smoothed particle hydrodynamics numerical settings

3.1.1 *The effects of particle spacing*

Known from literature [26], the shock profile predicted by SPH (particle velocity) is affected by the particle spacing when the applied constant to smooth length (CSLH) is fixed because the history variables at a particle (e.g., stress, strain, pressure, and particle velocity) are averaged based on the particle approximation. Figure 4 (a) shows the effects of particle spacing (p_c) on the particle velocity profile, with p_c selected between 0.3 and 1.0 mm. The minimum particle spacing is limited to 0.3 mm considering the exponentially increase in computational time when using a particle spacing of 0.2 mm or smaller. In Figure 4 (a), the particle spacing of 0.4 mm shows the closest prediction to the experimental measurement when compared to the lower and higher values. The maximum deviations at the peak velocity for $p_c = 0.3$ mm, $p_c = 0.4$ mm, $p_c = 0.6$ mm, $p_c = 0.8$ mm and $p_c = 1$ mm from the experimental result, are 0.5%. 0.1%, 7%, 17%, and 18%, respectively. Without considering the computational efficiency, a finer particle spacing trend results in a more accurate prediction of the particle velocity, which is consistent with other studies [21]. From Figure 4 (a), it is also observed that a larger particle spacing tends to shift the overall shock velocity profile towards the left, indicating a delay of the particle response. As a result, the obtained particle velocity is affected by the size of particle spacing with a fixed CSLH. To better illustrate the influence of the CSLH on the shock profile response, the observed trend for CSLH is shown in Figure 4 (b) with a fixed particle spacing of 0.4 mm. Figure 4 (b) shows the shock profile response is slightly affected by the CSLH at the Hugoniot state when the values of smooth length is less than 1.2. Lastly, it is noted that there is a seven times increase in computational time when the particle spacing decreases from 1 mm to 0.3 mm, as shown in Figure 4 (c).

To assess the effects of particle spacing on the predicted results of ballistic simulations, a series of particle spacing values covering the recommended range of 0.4 mm to 1.2

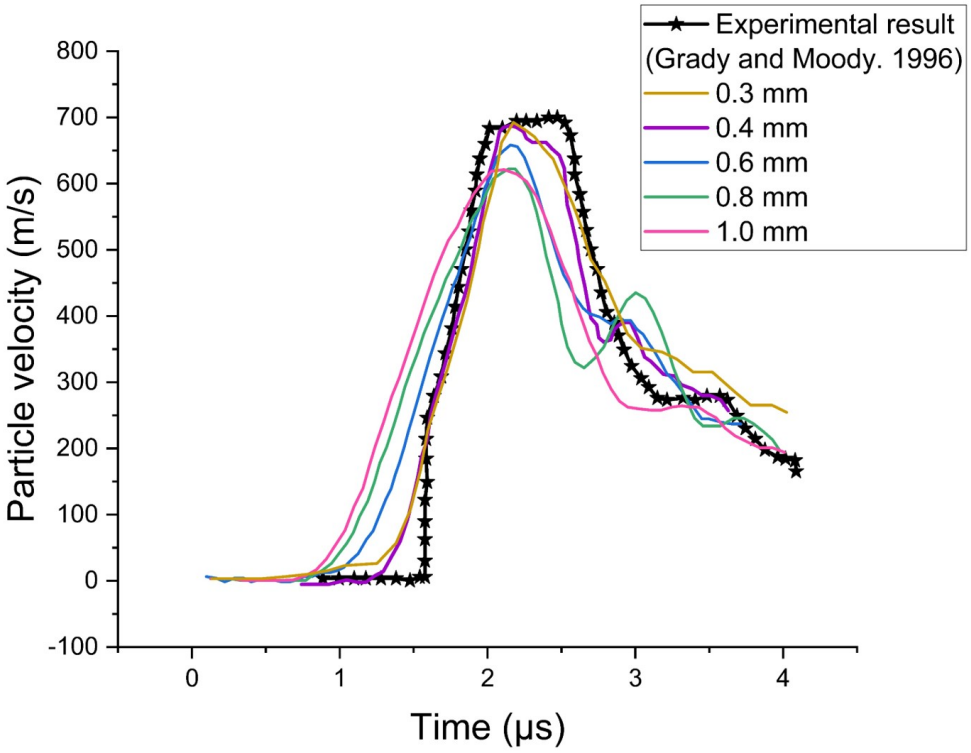
Experimental result
(Grady and Moody. 1996)
0.3 mm
0.4 mm
0.6 mm
0.8 mm
1.0 mm
Particle velocity (m/s)
Time (μs)

(a)

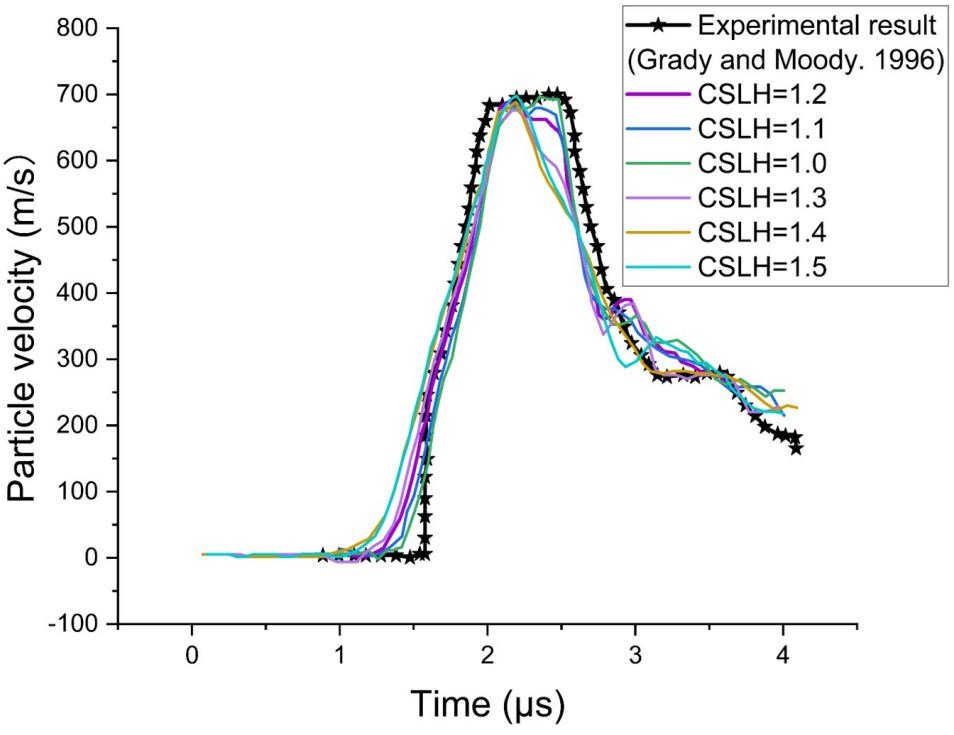
Experimental result
(Grady and Moody. 1996)
CSLH=1.2
CSLH=1.1
CSLH=1.0
CSLH=1.3
CSLH=1.4
CSLH=1.5
Particle velocity (m/s)
Time (μs)

(b)

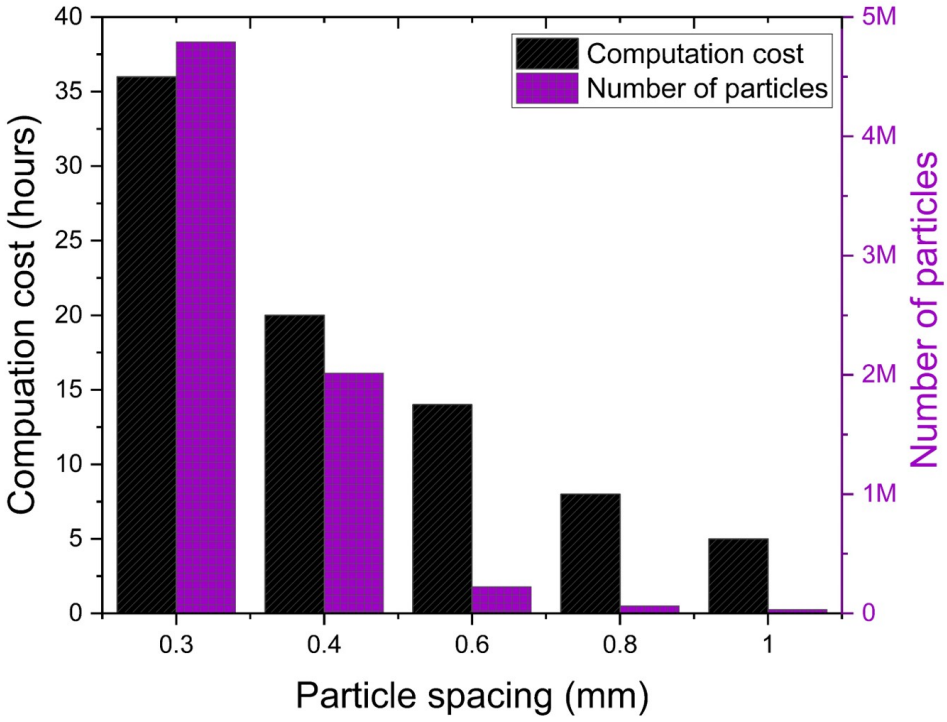

(c)

Figure 4: Sensitivity analysis of particle spacing and constant applied to smooth length and computational cost analysis of particle spacing used in the SPH framework for the impact configuration of Figure 3 at the striking plate velocity of 1070 m/s. (a) Sensitivity analysis on particle spacing with fixed CSLH=1.2: 0.3 0.4, 0.6, 0.8, and 1 mm. (b) Sensitivity analysis of constant applied to smooth length. (c) Computational cost for varying particle spacing with fixed CSLH=1.2. Experimental results are taken from Grady and Moody [22].

mm [17] are used with a fixed CSLH of 1.2. Figure 5 (a) shows the effect of particle spacing on the predicted residual mass and velocity of the projectile in ballistic impact simulations. In Figure 5 (a), the associated error bar at each particle spacing reflects the difference between the simulated and experimental results. Figure 5 (a) confirms that a reasonable prediction of residual velocity and mass of projectile can be reached when using a particle spacing between 0.4 mm and 1.2 mm, where a particle spacing of 1.0 mm gives the most accurate prediction with an associated error bar of 0.2%. The maximum deviations of the velocity for $p_c = 0.4$ mm $p_c = 0.5$ mm, $p_c = 0.8$ mm, $p_c = 1$ mm, and $p_c = 1.2$ mm from the experimental results, are 15.2% 13.5%, 5.4%, 0.2%, and 0.8% for the residual velocity prediction, respectively, and 11%, 10%, 8%, 0.3% and 0.7% for residual mass prediction, respectively. Generally, the trend demonstrates that the predicted projectile residual velocity and mass decrease with increasing particle spacing, and this trend is consistent with observations in other FEM simulations from the literature [17]. In previous simulations performed in an FEM framework, the mesh sensitivity has been mainly attributed the strain softening behavior which is widely observed in brittle materials [50, 51]. Such strain softening behavior leads to the strain and damage localization in a reduced volume after the mesh is refined [19]. In the SPH framework, the non-local effect is reduced with decreasing particle spacing, which leads to the strain

and damage becoming more localized, resulting in less global damage and resistance of the projectile penetration. This is evident in Figure 5 (a) where decreasing the particle spacing results in an increased residual velocity and mass of the projectile. A similar trend is observed for the CSLH where a decrease in the CSLH constant results in an increased residual velocity and mass of the projectile by fixing the particle spacing at 1.0 mm (see Figure 5 (b)). Finally, a trade-off should be often sought between computational efficiency and accuracy when choosing an appropriate particle spacing. For example, a twenty times increase in computational time is recorded when the particle spacing decreases from 1.2 mm to 0.4 mm (see Figure 5 (c)).

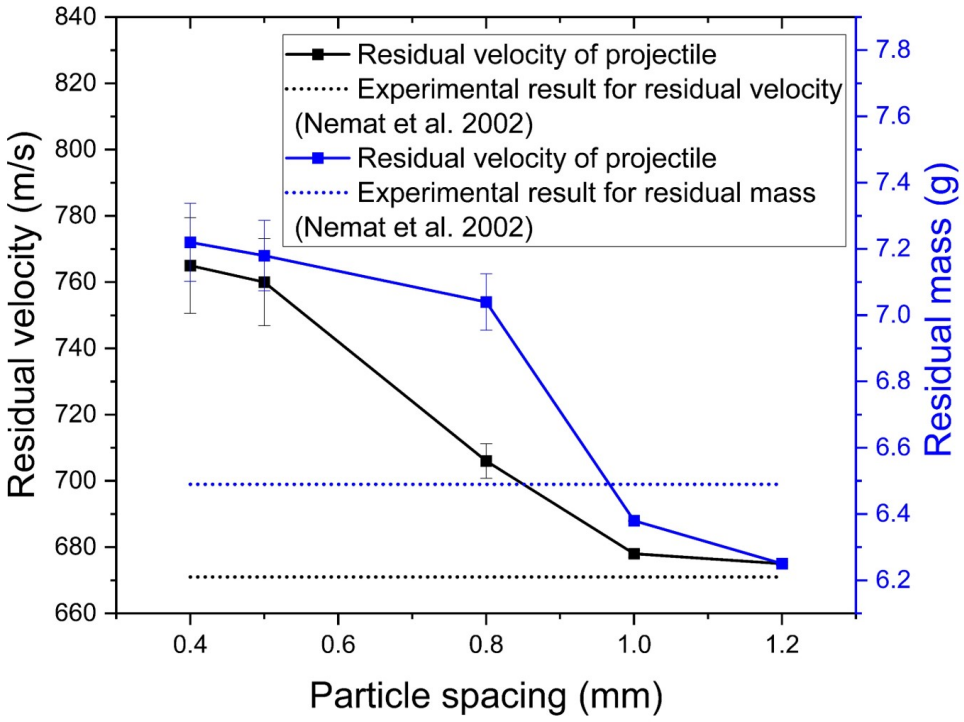
Residual velocity of projectile
Experimental result for residual velocity
(Nemat et al. 2002)
Residual velocity of projectile
Experimental result for residual mass
(Nemat et al. 2002)
Residual velocity (m/s)
Residual mass (g)
Particle spacing (mm)
840
820
800
780
760
740
720
700
680
660
7.8
7.6
7.4
7.2
7.0
6.8
6.6
6.4
6.2
0.4
0.6
0.8
1.0
1.2

(a)

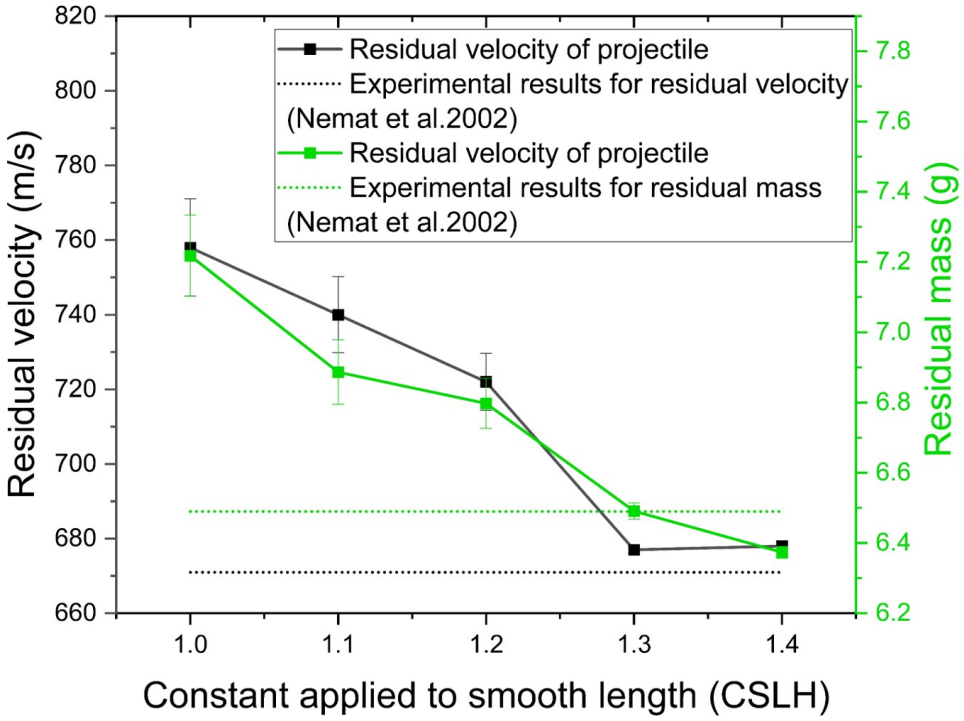
Residual velocity of projectile
Experimental results for residual velocity
(Nemat et al.2002)
Residual velocity of projectile
Experimental results for residual mass
(Nemat et al.2002)
Residual velocity (m/s)
Residual mass (g)
Constant applied to smooth length (CSLH)
820
800
780
760
740
720
700
680
660
7.8
7.6
7.4
7.2
7.0
6.8
6.6
6.4
6.2
1.0
1.1
1.2
1.3
1.4

(b)

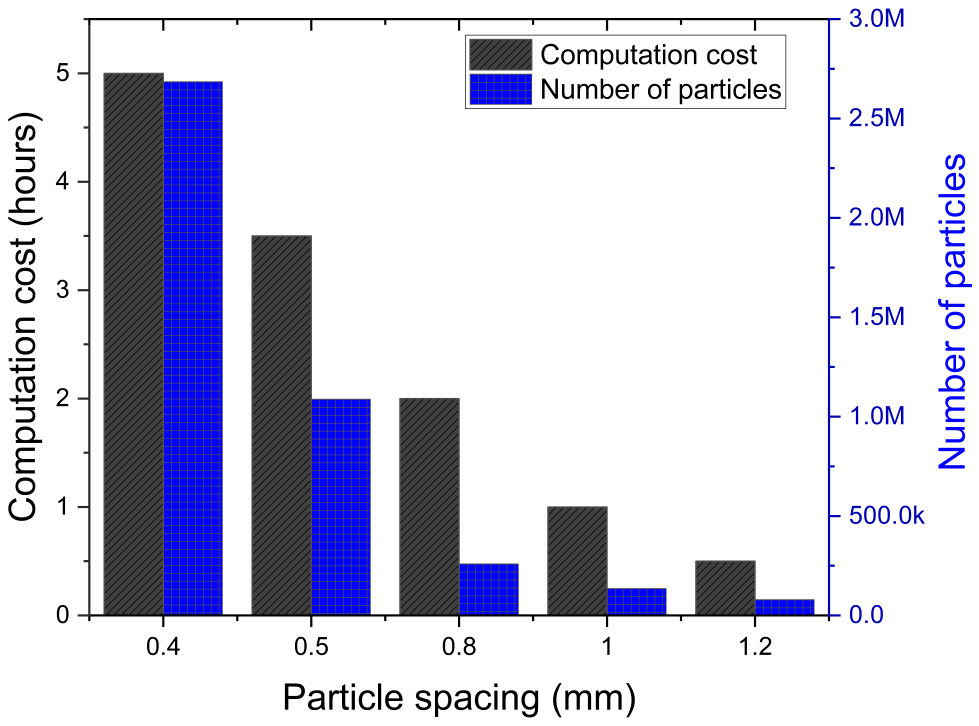

(c)

Figure 5: Sensitivity analysis of particle spacing and constant applied to smooth length and computation cost analysis of particle spacing used in the SPH framework for the impact configuration of Figure 4 at the projectile at an impact velocity of 901 m/s. (a) Sensitivity analysis on particle spacing with fixed CSLH=1.2: 0.4 0.5, 0.8, 1.0, and 1.2 mm. (b) Sensitivity analysis of constant applied to smooth length with fixed particle spacing of 0.4 mm=1.0, 1.2, 1.1, 1.3, 1.4, and 1.5. (c) Computational cost for varying particle spacing with fixed CSLH=1.2. Experimental results are taken from Nemat e t al . 2002 [41] .

3.1.2 *The effects of artificial viscosity*

Known from literature [26, 28], the predicted results are effected when strong discontinuities occur under the shock loading process. In SPH framework, artificial viscosity terms are introduced into the momentum and energy governing equations to prevent large unphysical oscillations and numerical instability under shock loading conditions [26]. Thus, the magnitude of artificial viscosity can affect the final simulation solution. In the current study, the effect of artificial viscosity on the numerical solution stability is investigated in the context of the plate impact simulations, with experimental data taken from Grady and Moody [22]. In the SPH framework, the artificial viscosity is defined as two terms: (1) the quadratic artificial viscosity term, Q1, which is primarily introduced to handle shocks generated at high Mach numbers [28], and (2) the linear artificial viscosity term, Q2, which is used to handle low gradient regions in the SPH simulations [28]. In this work, various combinations of Q1 and Q2 around the default LS-DYNA values (i.e., Q1 =1.5 and Q2 =0.06) are explored by fixing one value while varying the other to examine their effects on the plate impact simulations. Figure 6 (a) and (b) show the effects of Q1 and Q2 on the simulated shock profiles. It is observed that the simulated particle velocity is more sensitive to the Q2 values. The Q1 values only become dominant when the shock velocity becomes significantly large when compared to

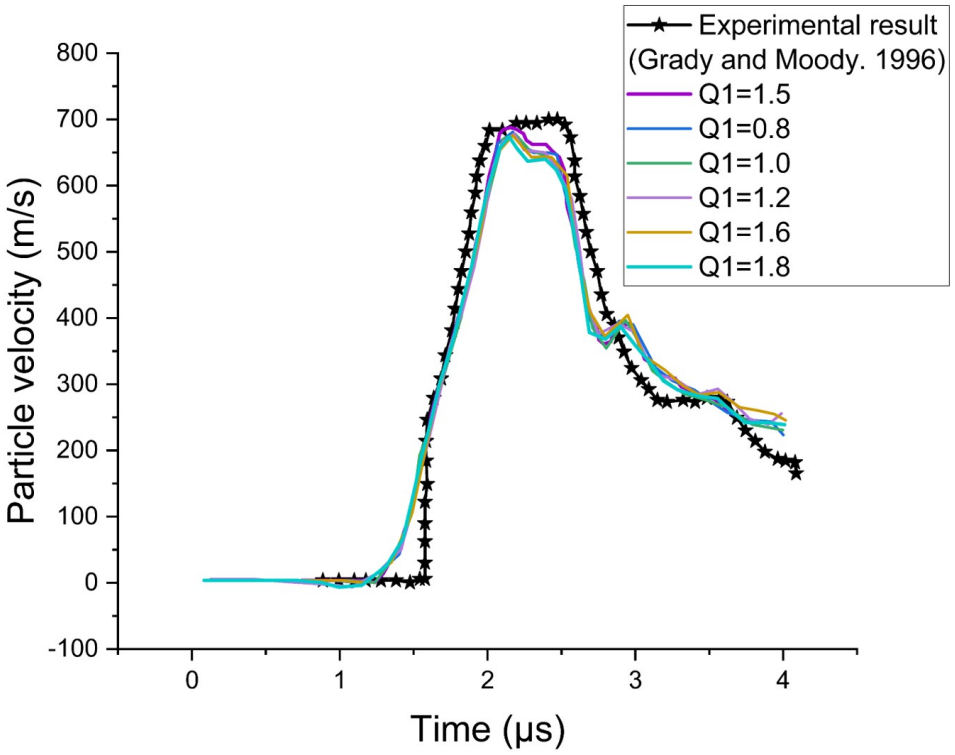
Experimental result
(Grady and Moody. 1996)
Q1=1.5
Q1=0.8
Q1=1.0
Q1=1.2
Q1=1.6
Q1=1.8
Particle velocity (m/s)
Time (μs)

(a)

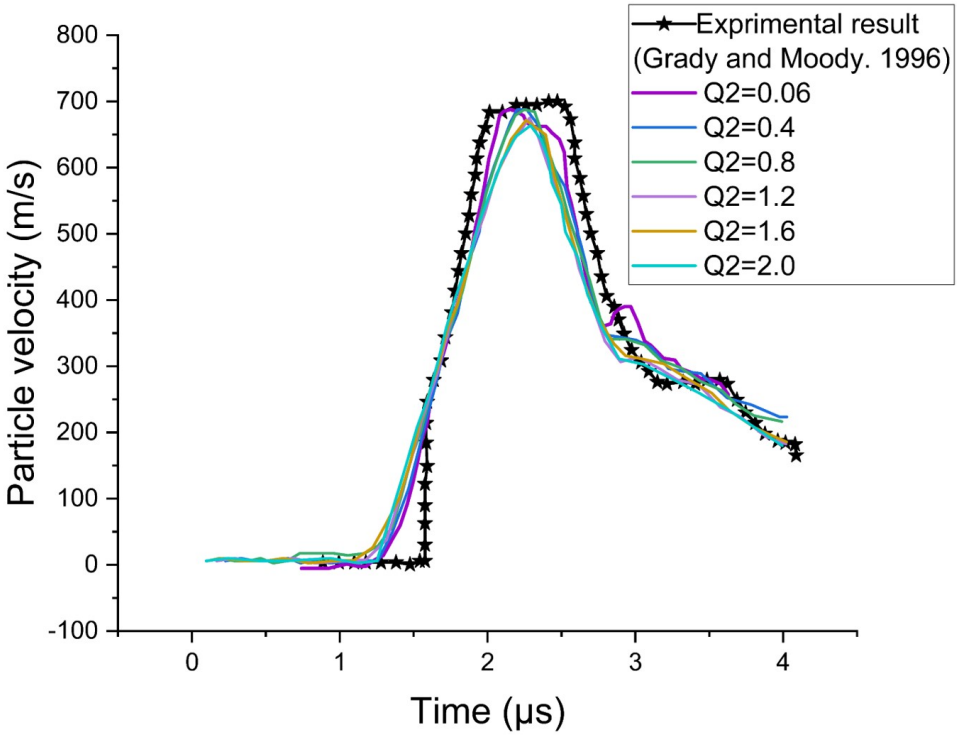
Exprimental result
(Grady and Moody. 1996)
Q2=0.06
Q2=0.4
Q2=0.8
Q2=1.2
Q2=1.6
Q2=2.0
Particle velocity (m/s)
Time (μs)

(b)

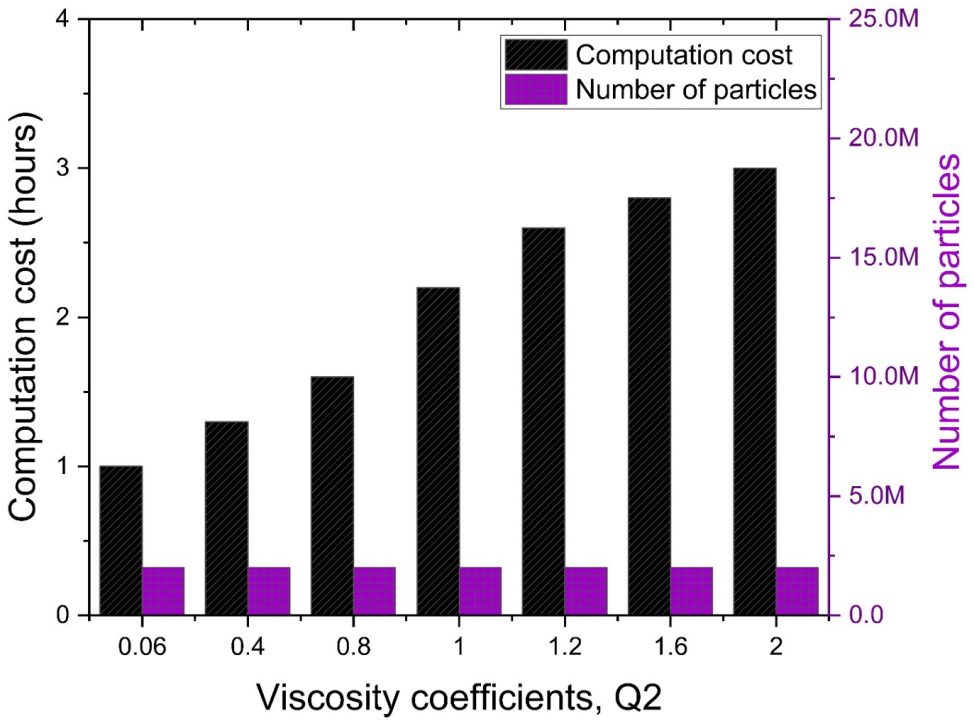

(c)

Figure 6: Sensitivity and computation cost analysis of artificial viscosity terms used in the SPH framework for the impact configuration of Manuscript Figure 3 at the striking plate velocity of 1070 m/s. (a) Sensitivity study on artificial viscosity Q1 parameters: 0.8, 1.0, 1.2, 1.5, 1.6, and 1.8 with fixing Q2 at 0.06 (default value in LS-DYNA). (b) Artificial viscosity Q2 parameters: 0.4, 0.8, 1.2, 1.5 with a fixed Q1 of 1.5 (default value in LS-DYNA). (c) Computation cost for varying Q2 with fixed Q1=1.5.Experimental results are taken from Nemat et al . 2002 [41]

sound speed in material, where the current simulations have a peak velocity range from 800 m/s to 1300 m/s in comparison with the sound speed of 10740 m/s [52, 53]. It is also noted that the computational time increase three times when changing Q2 from 0.06 to 2 (with Q1 fixed), and hence, a trade-off must be sought between computational efficiency and accuracy (see Figure 6 (c)).

A similar approach is used to examine the sensitivity of the artificial viscosity terms for the ballistic impact simulations (see Figure 7a). It is observed that the results for an impact velocity of 901 m/s have less than 4.4% of difference when varying Q1 from 0.4 to 1.5, where varying Q2 from 0.06 to 1.4 results in a difference up to 26.6% for both residual velocity and mass prediction. This confirms that the effect of artificial viscosity on both residual velocity and mass is greater affected by the linear artificial viscosity term Q2. For residual velocity, the simulated projectile residual velocity tends to decrease as Q2 increases (black curve with triangle on it in Figure 7a), where Q2 of 0.06 gives the most accurate prediction when compared to the experimental result [41] with an associated error of 0.5%. This trend is attributable to a enhancement of strength when Q2 increases, leading to more energy been dissipated, and resulting in a decreasing residual velocity [26]. For residual mass, the projectile residual mass increases with increasing Q2, and this is consistent with the trend observed in Xiao et al. [24], where the residual

mass tends to increase as Q2 increases. Overall, these observed trends demonstrate that projectile erosion is a complicated process and the ability for the material to erode the projectile may be related with fragment morphology [54, 55], friction between projectile and plate [54], and material strength [56, 57], and some of these link to energy dissipation. Finally, the computational time increase four times when changing Q2 from 0.06 to 2 (with Q1 fixed), and hence, a trade-off must be sought between computational efficiency and accuracy (see Figure 7b).

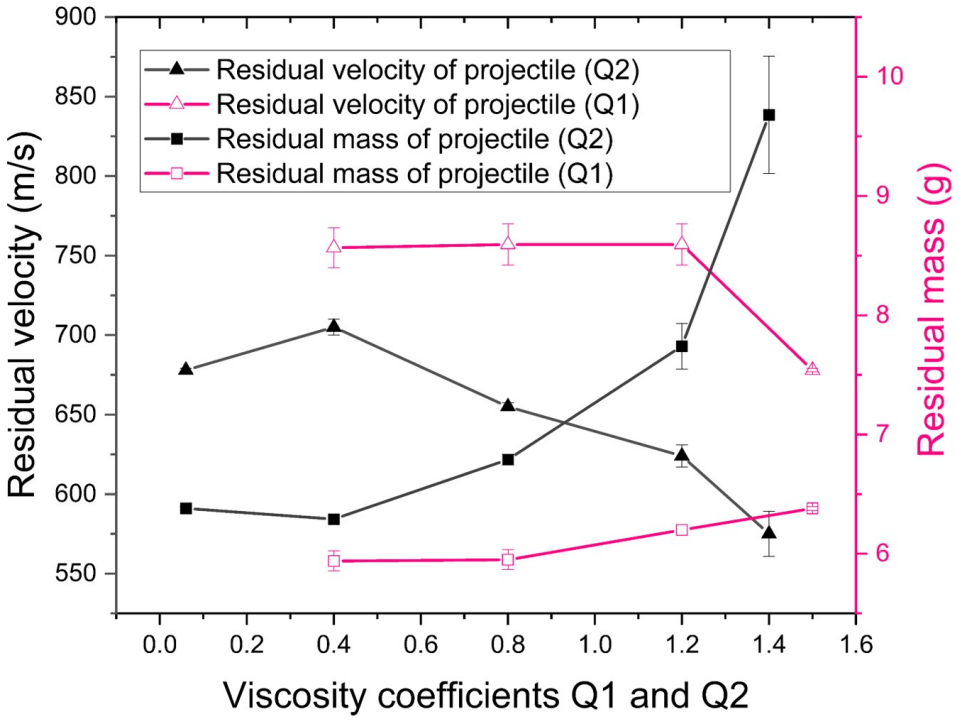

(a)

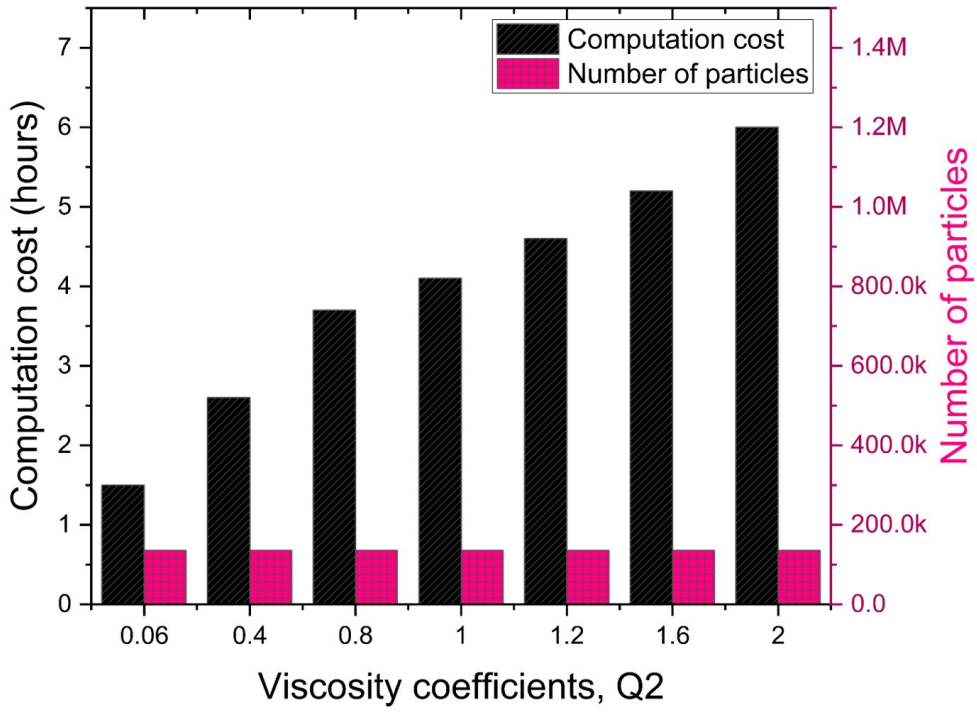

(b)

Figure 7: Sensitivity and computation cost analysis of artificial viscosity terms used in the SPH framework for the impact configuration of Figure 4 at the projectile at an impact velocity of 901 m/s. (a) Sensitivity study on artificial viscosity Q1 parameters: 0.8, 1.0, 1.2, 1.5, 1.6, and 1.8 with fixing Q2 at 0.06 (default value in LS-DYNA). (b) Artificial viscosity Q2 parameters: 0.4, 0.8, 1.2, 1.5 with a fixed Q1 of 1.5 (default value in LS-DYNA). (c) Computation cost for varying Q2 with fixed Q1=1.5.Experimental results are taken from Nemat et al . 2002 [41].

3.2 Plate impact and ballistic impact simulations

The plate impact test is an experimental technique used to study the shock response of ceramics and inform the values of the Hugoniot elastic limit (HEL), spallation strength, and equation of state (EOS) parameters [45, 52, 58, 59]. Figure 2 shows the simulation setup of a typical plate impact test, following the configuration provided in Grady and Moody [22], with dimensions varying in our simulations according to Grady and Moody [22] in order to generate different shock velocities. In this study, a particle spacing of 0.4 mm is used in our simulations (e.g., 2015254 particles involved when impact velocity is 1070 m/s), where this value is chosen based on the results from sensitivity studies (see Section 3.1.1 for details). Here, the responses of the alumina impactor and target are characterized using the same material constants of the JHB model as shown previously in Table 1. The response of the lithium fluoride (LiF) block is defined using a Steinberg-Guinan material model and Mie-Grüneisen EOS [15]. In the Steinberg-Guinan model, the reference yield strength (A_s) and the shear modulus (G_s) of the lithium floride block was chosen as A_s=0.36 GPa, and G_s=49 GPa at T_s = 300 K, P_s = 0 GPa, and ϵ_{pls} = 0, where the subscript S is added because of repeated notations. The other material constants of LiF and computational parameters are provided by Sukanta et al.[60], and these are summarized in Table 2.

Table 2: Steinberg-Guinan material model constants for lithium fluoride window block in plate impact simulation [60].

Model Parameters	Notation	Value
Density (kg/m^3)	ρ_l	3890
Bulk modulus (GPa)	K_l	265
Strength parameter (GPa)	dG/dp	2.45
Strength parameter (GPa)	dG/dT	0.0303
Melting temperature (K)	T_{ml}	1480
EOS Parameters		
Gruneisen coefficient	G_c	1
Linear Hugoniot slope coefficient	S_1	0.005
Bulk speed of sound (m/s)	C_1	5150

Figure 8 shows the comparisons between the experimental and simulated plate impact results with striking plate velocities of 1070 m/s, 1551 m/s, 1573 m/s, and 1911 m/s. The plate impact experimental results are provided by Grady and Moody [22], and three different geometric configurations of the experimental setup are investigated in this study (configurations denoted in the caption of Figure 8). Figure 8 (a) labels the critical stages of the typical material response during a plate impact experiment: (1-2) elastic response up to HEL; (3-4) inelastic response up to the Hugoniot state, where the Hugoniot state describes the locus of all final shocked states (pressure–volume relationship) in a material for various maximum pressure values [61]; and (4-5) the shock release undergoes unloading where tensile stress are built up during the elastic unloading, leading to spalling of the material [61]. From Figure 8 (a)-(d), it is observed that the model reasonably captures the shock profile from Grady and Moody [22], with some differences noted in the stage (1-2) up to HEL and the plateau at peak velocity, where differences likely stem from the numerically-introduced artificial viscosity in the SPH framework [27]. The experimental

results are reasonably validated when compared with other such approaches made in the literature [21], where it has been observed that impact velocity does not greatly affect the HEL [62, 63], and increasing impact velocity results in greater amplitude and slope of the plastic front [62, 63].

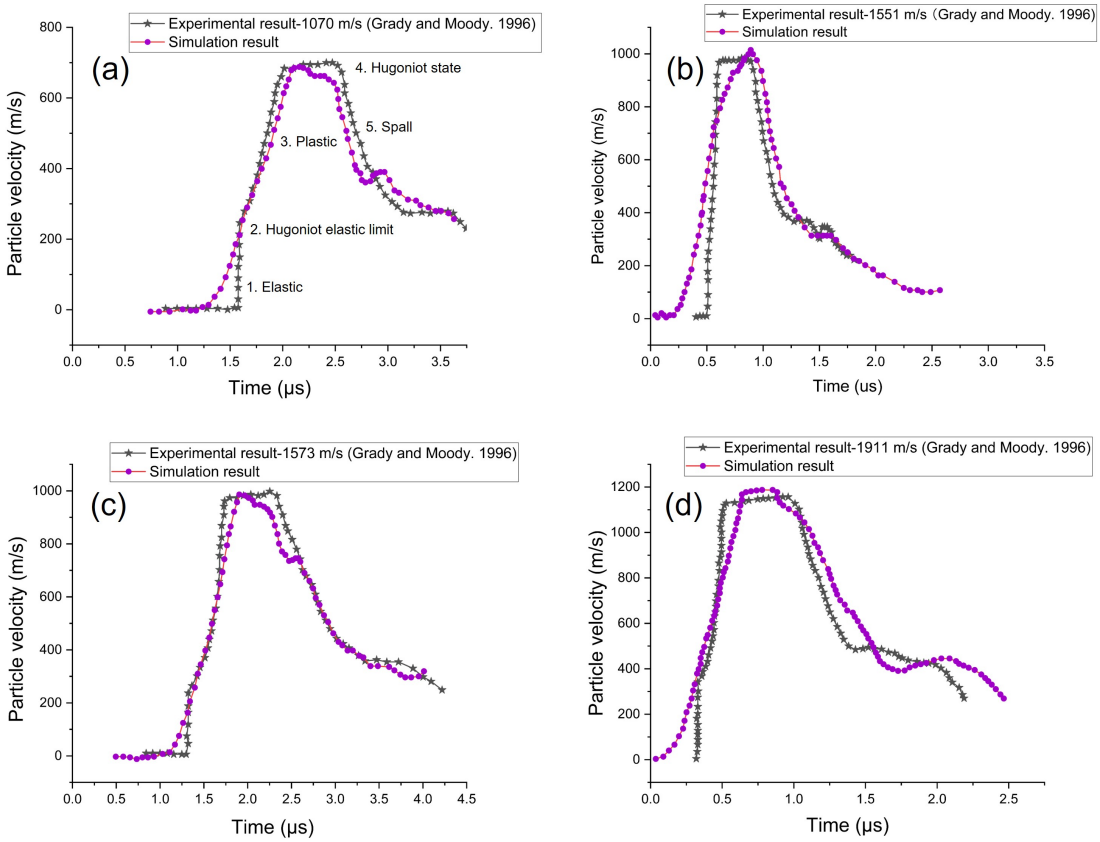

Figure 8: Comparisons between experimental and simulated plate impact results : histories of the particle velocity captured at Point B (see Figure 2) for the striking plate velocity = 1070 m/s (a), 1551m/s (b), 1573 m/s (c), and 1911 m/s (d) based on JHB model. The experimental data is taken from Grady and Moody [22]. (a,b): alumina sample D: 76.2 mm, T: 10 mm, alumina impactor D: 87.5 mm, T: 5 mm, lithium fluoride window block D: 50.8 mm, T: 25.4 mm, (c): alumina sample D: 76.2 mm, T: 4.762 mm, alumina impactor D: 76.31 mm, T: 2.475 mm, lithium fluoride window block D: 38.1mm, T: 25.4 mm. (d): alumina sample D: 76.3 mm, T: 2.478 mm, alumina impactor D: 76.2 mm, T: 2.477 mm, lithium fluoride window block D: 38.1mm, T: 25.4 mm.

In addition, the implementation of the Johnson-Holmquist-Beissel model along with the best combination of SPH parameters is also quantitatively and qualitatively matched and compared with ballistic impact data from the literature [41]. Specifically, the quantitative data is in the analysis of the residual velocity and mass of the projectile after penetration, while the qualitative comparisons are performed by matching time resolved X-ray images provided in Nemat-Nasser et al. [41]. Figure 3 shows the configuration of the SPH-based model corresponding to the ballistic experiment performed by Nemat-Nasser et al. [41] involving a tungsten alloy long rod impacting on a single alumina tile. In this setup, the ceramic tile is made of 99.5% purity alumina and has dimensions of 101.6 mm×101.6 mm×12.7 mm. The tungsten heavy alloy projectile has a diameter of 6.14 mm and a length of 20.86 mm (see the front view in Figure 3), and the impact velocities of the projectile are 901 and 904 m/s. The alumina tile is described using the same

JHB model parameters provided in Table 1. The Johnson-Cook strength and damage model constants of the projectile are provided in Table 5 [42] (See Appendix A).

Table 3 summarizes the results of the simulated and experimental impact data, including the residual velocities of projectile, the mass, and relative error between the simulation results and experimental measurements. The residual velocity of the projectile in the simulation is taken at the resultant rear center node of the projectile. The residual mass of the projectile in the simulation is calculated as the difference between the initial projectile mass and mass of the fully damaged projectile particles upon penetration. The damaged projectile particles are simulated by setting (`EROD=2`) in the (`*CONTROL_SPH*`) card of LS-DYNA. Here, the "smooth" option is selected in LS-DYNA PrePost to distinguish between the activated and deactivated particles. From Table 3, for both impacting velocities, the model predictions show good agreements with the experimental results by Nemat-Nasser et al. [41], with relative errors within 6% for both residual velocities and masses. The proposed model performs significantly better than those reported in the literature for similar impact conditions [42], where most of them showed relative errors of greater than 20% for the residual mass prediction [42]. For example, Bresciani et al. [42] showed 33% error against experimental results with a cohesive model for the same impact case.

Table 3: Comparisons between experimental results from Nemat-Nasser et al. [41] and simulated results in predicting the residual velocity and residual mass for the projectile impacting an alumina tile with the implemented Johnson-Holmquist-Beissel model [20]

Experiments	Impact velocity (m/s)	Residual velocity of the projectile (m/s)	Residual mass of the projectile (g)
Experiment 1 [41]	901	671	6.49
LS-DYNA	901	686	6.11
Error (%)		2.23	5.84
Experiment 2 [41]	904	682	6.42
LS-DYNA	904	689	6.1
Error (%)		1.02	4.98

Furthermore, the nature of the mesh-less feature of the SPH method allows to simulate severe deformations and fragmentation of both the projectile and ceramic tile without defining element erosion [42, 47] and the use of cohesive elements [42]. In turn, these advantages of the SPH method allow more accurate qualitative replication of the ballistic events (e.g., debris cloud [47] and back-face spallation [64]). Figure 9 (a) shows the simulated residual velocity vs. time curve for the impact condition of initial velocity of 901 m/s with times denoting selection of still frames from experiments by Nemat-Nasser et al. [41](X-ray images) and models shown in: Figure 9(b) for 7 μs with a residual velocity of 840 m/s, and Figure 9(c) for 15 μs with a residual velocity of 779 m/s. Overall, the computational framework implemented in this work can reasonably capture the damage evolution process and failure modes when the projectile penetrates the ceramic target. For example, deformation and erosion of the projectile, target spallation, material pulverization into fine powder, and ejection of the debris cloud occurs from both front and rear target surfaces. More simulated damage evolution images of ceramic tile and projectile are provided in Figure 15 of the Supplementary Material section.

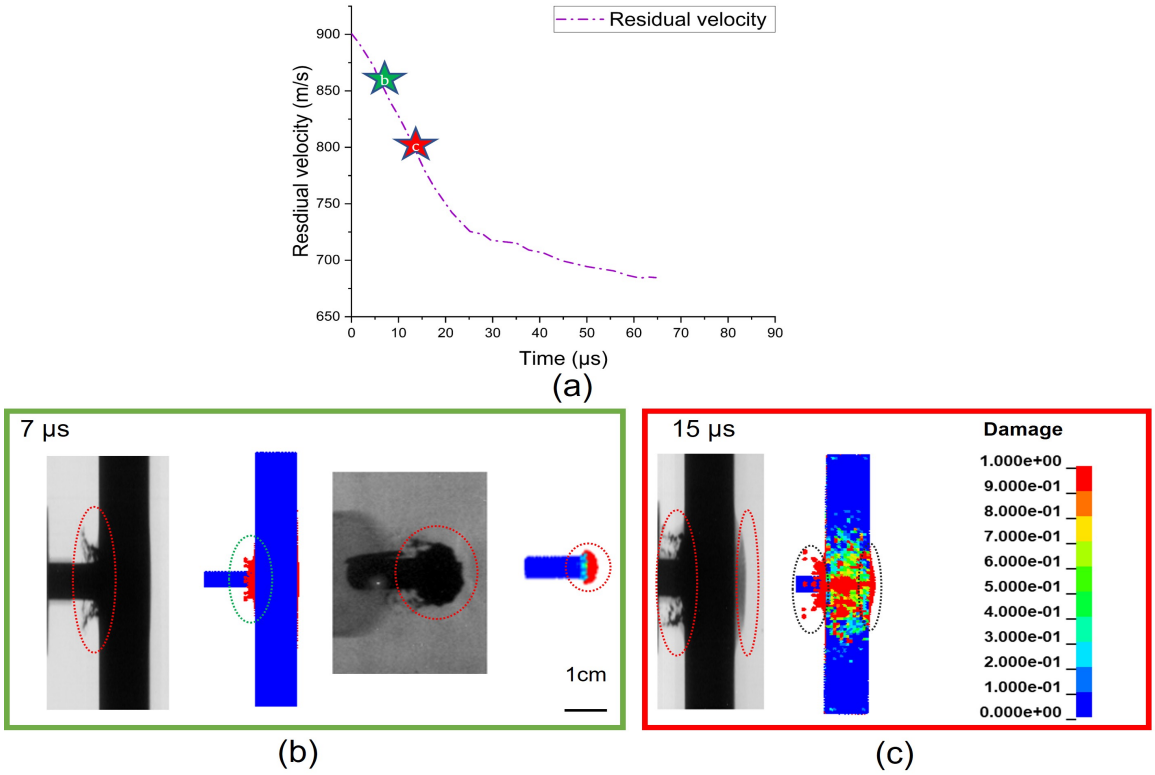

Figure 9: Comparisons between the simulated results and time-resolved experimental flash X-ray images [41] during a long rod impact at 901 m/s. Plot of the residual velocity of projectile vs. time with noted time points identified for comparing simulation and experimental results of the tile and projectile are compared at: (b) 7 μs and (c) 15 μs.

4. Multi-layer perceptron model and sensitivity analysis

In this section, a multi-layer perceptron (MLP) model has been developed to statistically explore the non-linear relationships between inputs (e.g., shear modulus, material strength, thickness, and impact velocity) and performance (i.e., residual velocity and mass of the projectile) in the situation of a projectile impacting a single alumina tile.

Here, the residual mass and velocity are two common performance metrics used in literature [10, 42, 43, 65]. Other performance metrics such as dwell and penetration may also be used, although the literature is much more limited [56, 66].

4.1 Architecture of the neural network

The topology of the proposed MLP model (see Figure 10) is characterized by grouping neurons in the input layer (1), hidden layers (4), and output layer (1) following the work by Parsazadeh et al.[67]. The input layer consists of the most influential variables which are thought to have significant effects on the material performance during ballistic impact events (e.g., tensile strength), and this will help gain a better understanding of the physical phenomenon during impact. Specifically, important characteristics such as the thickness of the ceramic tile, impact velocity of the projectile, and material strength parameters for both ceramic and projectile that may affect the ballistic performances (i.e., residual mass and velocity) are included in the training of the MLP model. For geometries (e.g., thickness of ceramic tile, impact velocity of projectile), these represent simple and standard considerations based on literature [66, 68, 69]. Additional geometric variables could be considered for the target (e.g., hexagonal geometries [70], spatial arrangements [7], lattice structures [71, 72]) and projectile (e.g., nose and fin geometries [73], sphere [74] vs. rod [42]) in future works. For mechanical properties (e.g., compressive and tensile strength of ceramic, shear modulus), these represent simple and physically significant choices that have been studied previously in the literature [68, 69, 75]. Additional properties could be considered (e.g., Poisson's ratio, damage constants [19, 20]), including those that are dependent on the FEM scheme of choice (e.g., fracture toughness in discrete-element framework [76], defect populations and crack speeds in micro-mechanical models [77]). Each input parameter has a range associated with them, which is surveyed from literature and demonstrates both the material variability in properties (e.g., max intact strength) and typical configurations of ballistic impact experiments (e.g., impact velocity) [78]. Figure 10 illustrates a complete list of the inputs and Table 4 summarizes the references for the ranges. Four hidden layers with 32 neurons at each layer have been determined through the trial-and-error approach given the accurate prediction and then assigned to the ML model [67]. In this study, the MLP model is trained using the forward and backward propagation algorithms. The Relu function is adopted in the forward algorithm as the activation function to output the non-linearity at each layer. The Relu function is chosen because of the nature of its differentiation form which allows the computation to overcome the vanishing gradient problem by keeping high computational efficiency [79]. In conjunction with forward propagation, the Bayesian regularization back-propagation is used for computing the gradient in the weight space of the MLP model with respect to a loss function [79]. Finally, the RMS-propagation algorithm is then used to minimize the error by updating the weight and bias values of the MLP model [80]. Relevant equations for the MLP were described previous in Appendix A.

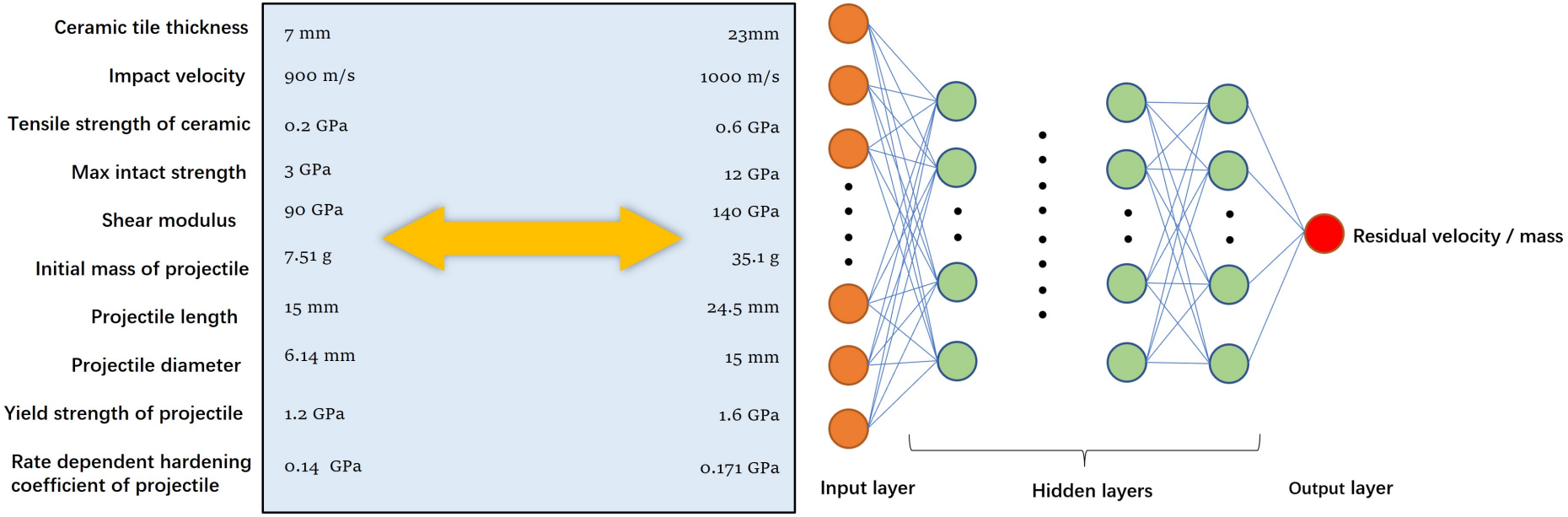

Figure 10: Architecture schematics of multiple perceptron model showing the all the input variables considered for ballistic impact case (left) associated with identified parameter range from literature (middle), and construction of the MLP with output of residual velocity and mass of the projectile (right).

Table 4: Input variables for MLP model associated with a range that is identified from the literature.

Model Parameters	Notation	Value Range
Ceramic thickness (mm)	t	7 to 23 [17, 48]
Impact velocity (m/s)	V_i	700 to 1000 [10]
Tensile strength of ceramic (GPa)	T	0.2 to 0.6 [64, 81]
Maximum intact strength (GPa)	σ_{max}	3 to 12 [47, 82]
Shear modulus (GPa)	G_p	90 to 140 [17, 64]
Initial mass of projectile (g)	m_i	7.51 to 35.1 [42]
Projectile length (mm)	l	15 to 24.5 [42]
Projectile diameter (mm)	D_p	6.14 to 15 [42]
Yield strength of projectile (GPa)	A	1.2 to 1.6 [24, 83]
Rate dependent hardening coefficient of projectile (GPa)	B_p	0.14 to 0.171 [24, 83]

4.2 Training, validation, and testing of the multi-layer perceptron neural networks

Next, we train, validate and test the MLP model within the Python environment. The sample size covers the ranges shown in Table 4. The required number of samples for training, validation, and testing is determined through a trial-and-error approach until the prediction variation is less than 10% for convergence. The total required sample size for training, validation, and testing started with 188 samples with bad prediction performance for interesting ranges of input parameters. We gradually increased the sample size to 320 and a good prediction performance was obtained because of the generalization of sample size. The sample size of 320 is generated to train, validate and testing the MLP model using the validated SPH model by randomly varying any input parameters while keeping others fixed within the defined ranges shown in Figure 10. This approach is common in literature [38, 39, 84]. Then, the generated data are randomly assigned into training, validation and testing sets by following the training-validation-testing split method with a ratio of 80:10:10 [84]. The training-validation process uses the Mini-Batch RMS-propagation algorithm [85] to achieve the best training stability and generalization performance with normalized inputs and output. The batch size is defined as 32 [86], along with epochs of 200. A batch size of 32 is commonly recommended in literature because it is practically efficient in computing the matrix-matrix products over matrix-vector products [86, 87]. The RMS-propagation algorithm run with default values of learning rate = 0.001, gradient moving average decay factor (rho) = 0.9 [86]. The training and validation performance is evaluated using the mean square error loss function [86]. An early stopping criterion is also considered during the training process for stopping the ML model overfitting. The model will stop for training if a bad degraded performance is observed (mean sqaure error goes up) during the validation process [86]. Figure 11 shows the results of training, validation, and testing capabilities of the proposed MLP model. Figure 11 (a) and (b) shows the mean squared error vs. epochs plot for training and validating the MLP model, with a continuous and rapid decrease in the mean square error (MSE) close to zero for the predicted residual velocity and residual mass, respectively. Both of these plots indicate a well trained and validated MLP model has been achieved [38]. Figure 11 (c) and (d) are predicted values vs. actual values plots showing the comparable accuracy of the MLP model to SPH simulation in predicting the residual velocity and mass of projectile based on testing-split data (experimental and numerical data). In the figures, the center diagonal line indicates a perfect match between the predicted and

true values, and the more points close to the diagonal line indicates a better prediction. From the figure, it is observed that the proposed MLP model can predict both residual mass and residual velocity with less than 7% of absolute percentage error compared to the SPH model (purple dots), with simulation results of experimental data shown in green (see Figure 11 (c) and (d)). The computational time for MLP prediction is only 800 ms, and this is compared to approximately of two hours for the SPH simulations. The observed outliers in the plot (e.g., two points in Figure 11 (c) and three points in Figure 11 (d)) suggests further detailed error analysis on data-noise and model architecture needs to be performed to improve model prediction. Altogether, the MLP model in the current work showcases a clear path that can be used to develop such efficient machine learning models for generating accurate predictions for a specific loading case encompassing wide ranges of conditions.

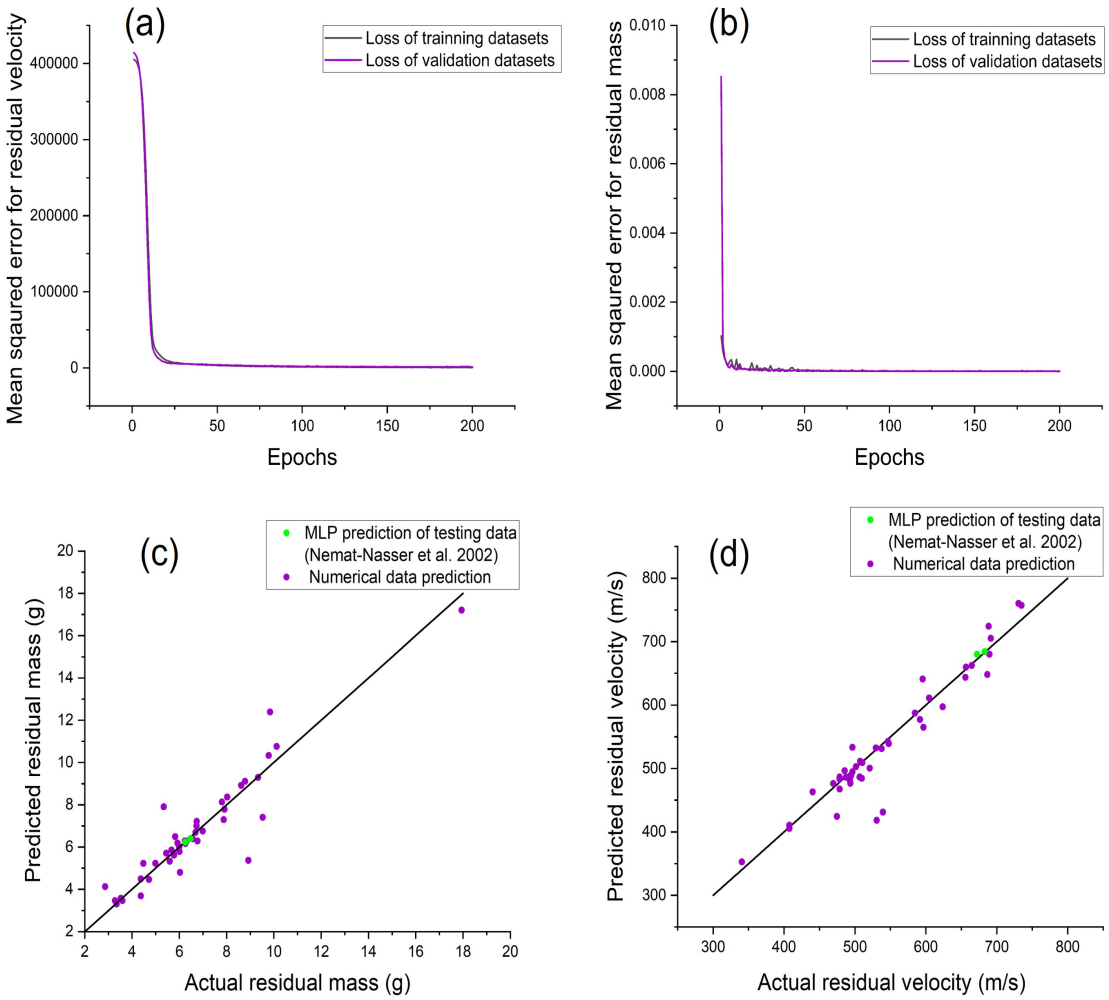

Figure 11: Training, validation, and testing of the multi-layer perceptron model. (a) The mean squared error plot shows the well-trained and validated multi-layer perceptron model for the residual velocity. The model is trained and validated through train-validation-split datasets with a ratio of 80:10:10. (b) The mean square error plot shows the well-trained and validated multi-layer perceptron model for residual mass. (c) A prediction vs. actual plot for the residual velocity shows the capability of the model in predicting the residual velocity of projectile based on the testing-split dataset. (d) A prediction vs. actual plot for the residual mass shows the capability of the model in predicting the residual mass of projectile based on the testing-split dataset (the diagonal line represents an excellent match).

4.3 Sensitivity analysis using multi-layer perceptron

Next, parametric studies are carried out to investigate the effects of mechanical properties (e.g., strength and shear modulus) and geometries (e.g., tile thickness) of the alumina ceramic tile on its ballistic performance by using the well-trained MLP model. Typical parameters, including impact velocity of the projectile, thickness, tensile strength [88], maximum intact strength [56, 57], and shear modulus [88] of the alumina ceramic tile are selected to be analysed in this work because of their noted influences on ballistic performance [56, 69].

Shown in Figure 12 are the results of the parametric studies on residual velocity (a) and residual mass (b) of projectile by varying the corresponding parameters over the assigned range (see Table 5). Note that the inputs are normalized on the x-axis based on the average of values for the ease of comparison. Data points are plotted as averages with standard deviations from five simulations using the MLP model for given parameters of interest. Trends in Figure 12 (a) demonstrates that the residual velocity decreases with the increase of thickness, maximum intact strength, and tensile strength of the ceramic tile, with a higher sensitivity for the intact maximum strength and thickness parameters. These trends and sensitivities are consistent with the experimental results from literature (i.e, tensile strength [68, 75], intact maximum strength [69], and thickness [88]). For example, the intact maximum strength (i.e., compressive strength) often plays an important role in the ballistic performance of ceramics because of the compressive and shock waves generated failure during impact [61]. Similarly, Figure 12 (b) shows the sensitivity of residual mass to thickness, impact velocity, maximum intact strength, shear modulus, and tensile strength. Residual mass is metric of projectile defeat through erosion [89]. From the plot, a clear trend of decreasing residual mass is seen for an increasing impact velocity and thickness, which is consistent with the literature (i.e. impact velocity [66] and thickness [66]. Note that a similar trend for the tensile strength is observed for the residual velocity (see Figure 12 (a)) and residual mass (see Figure 12 (a)), and further investigations are needed to identify the roles of possible physical phenomena (e.g., the commonly denoted fracturing from the reflected tensile waves at the free surface of the ceramic tile [84]) and numerical effects. Regardless, the residual mass appears to be less sensitive to tensile strength with no previous literature available to confirm this observation. Finally, the shear modulus exhibits non-linear decreasing-increasing trends for both the residual velocity (Figure 12 (a)) and mass (Figure 12 (b)), which is either: (1) associated with the interplay between impact physics (e.g., dwell [11, 12], wave propagation [61], and damage accumulation [49, 89, 90]); (2) the constitutive model construction (i.e., see Equation (11) in the JHB material model). Further experimental data and explicit failure modeling of impact phenomena [91–93] are needed to unravel individual effects of these input parameters.

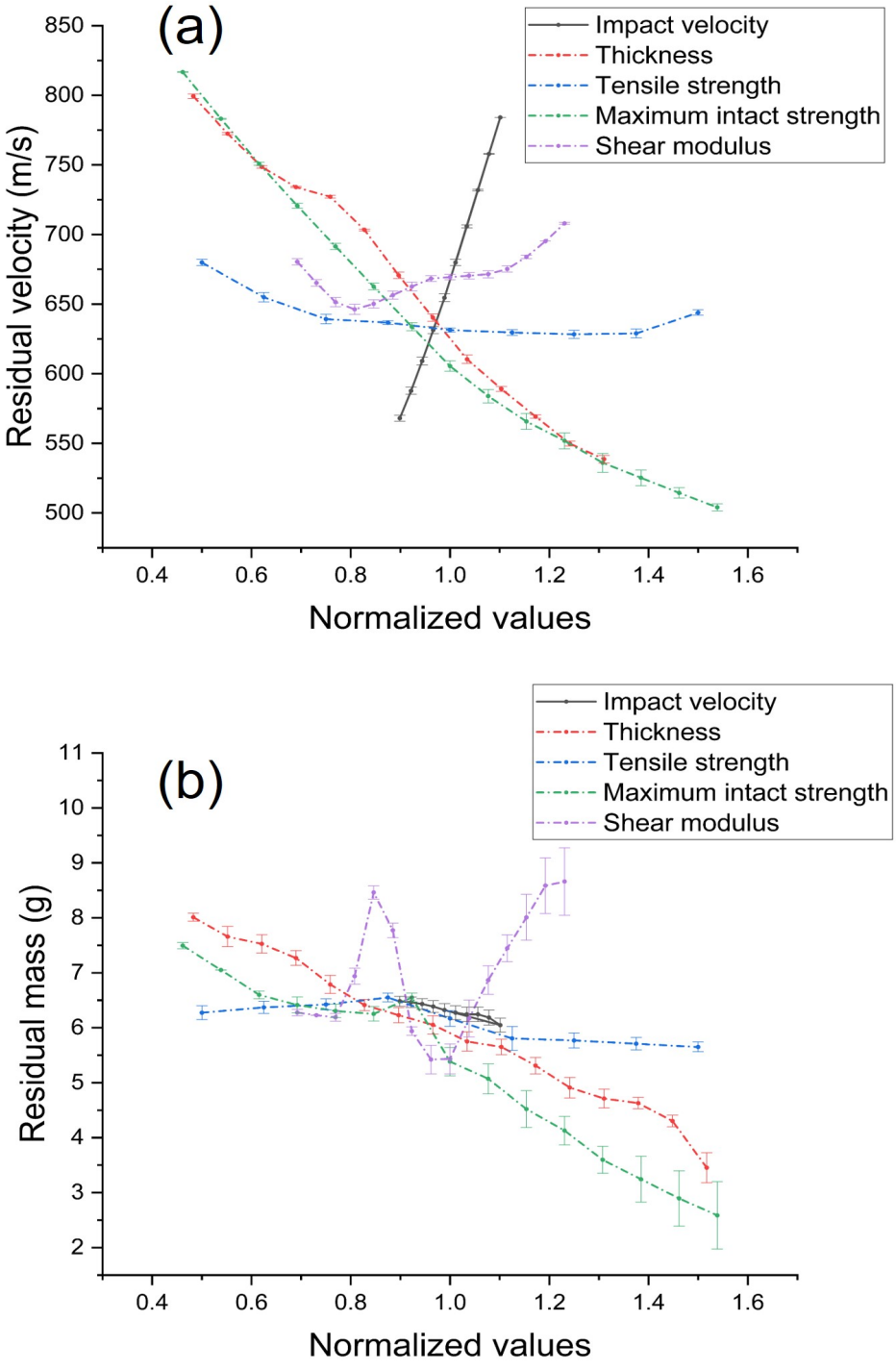

Figure 12: Sensitivity analysis for studying the effects of mechanical properties (tensile strength, maximum intact strength, and shear modulus) of the alumina ceramic tile and geometries (thickness and impact velocity) on the: (a) residual velocity and (b) mass of the projectile by using the multilayer perceptron model.

5. Conclusions

This study has developed a combined computational framework based on the smoothed particle hydrodynamics (SPH) and machine learning algorithms for investigating impact responses of an alumina ceramic, in which the Johnson-Holmquist-Beissel (JHB) material model was implemented into the LS-DYNA through a user-defined subroutine to account for high pressure, high strain rate, and damaged behavior during plate impact and ballistic loading. The implementation of the JHB model was verified by comparing the equivalent stress-pressure plots through a single element simulation test. The JHB model material constants were inferred and calibrated based on data from the literature. The developed computational framework demonstrated a good agreement between the numerical and experimental results, both quantitatively (e.g., particle velocity signal, residual velocity, and residual mass of the projectile) and qualitatively (e.g., debris, spall, cone, mushrooming deformation, and erosion of the projectile). A comprehensive sensitivity analysis on the SPH numerical settings was then conducted and revealed that the change of particle spacing could result in 12% and 17.2% change in residual velocity and mass of projectile, respectively, but with a six times increase in computational time. Lastly, the developed neural network model as an alternative to SPH model demonstrated that an accelerated prediction and optimization of the performance characteristic for ballistic impact case with reasonable accuracy. Overall, the proposed combined SPH-MLP approach and the associated analysis provide an alternative path for high throughput identification and insights into the property and performance relationships, which is applicable to structural-scale design of ceramic-based protection systems.

Acknowledgments

This work is supported by Defence Research and Development Canada (DRDC), General Dynamics Land Systems-Canada, and NP Aerospace through NSERC Alliance project ALLRP 560447-2020. We thank Geneviève Toussaint of Defence Research and Development Canada for feedback and support that led to the publication of this study. The views and conclusions contained in this document are those of the authors and should not be interpreted as representing the official policies, either expressed or implied, of General Dynamics, NP Aerospace, DRDC or the Government of Canada. The Government of Canada is authorized to reproduce and distribute reprints for Government purposes notwithstanding any copyright notation herein.

Supplementary Material

This section provides the detailed descriptions of Johnson-Holmquist-Beissel model (JHB) used in this work, material constants for Johnson-Cook material model, and a flow chart used for defining the implemented computer code for the present study (see Appendix A). In addition, it also provides the results (see Appendix B), are including: (1) a single element verification used fo checking the accuracy of the implementation of the JHB material model into finite elemnt code in LS-DYNA. (2) a damage evolution image for both the alumina ceramic tile and the projectile under ballistic impact velocity of 901 m/s (see Figure 15).

Appendix A: Numerical methods

In this work, a finite element model has been implemented in LS-DYNA software within the framework of smoothed particle hydrodynamics (SPH) [24, 26] by adopting the Johnson-Holmquist-Beissel (JHB) constitutive model for ceramics, the Johnson-Cook (JC) material model, and Gruneisen equation of state for a tungsten long rod projectile. LS-DYNA software has been chosen in the present study as it is better suited for large-scale dynamic simulations with consideration of inertia effects for dynamic impact problems [94]. Even though LS-DYNA has a large variety of material models (e.g., explicit dynamic models) and contact algorithms (e.g., eroding contacts and tied surfaces contacts) [94], the JHB model is currently not available in the LS-DYNA software and has to be written through a user-defined sub-routine. Hence, the proper implementation and verification of the subroutine is essential before carrying out any impact simulations. A flow chart used for defining the implemented computer code for the present study is included (see Figure 13). Lastly, this section presents the structure of an artificial neural network tool based on multilayer perceptron (MLP) method for predicting predicting and investigating the effect of mechanical properties and geometries on material performance.

Johnson-Holmquist-Beissel model for alumina ceramic

The Johnson-Holmquist-Beissel model (JHB) [20] has been selected to describe the mechanical responses of the alumina ceramic in this work. The JHB model consists of three main components: (1) a strength material model, (2) a damage model, and (3) an equation of state model that considers the phase change of materials [20, 21]. When compared to the previous JH models [18, 19], the differences of the JHB model are [20]: (1) a piece-wise strength-pressure and damage-pressure envelope is included, (2) the pressure and strain-rate independent response beyond the Hugoniot elastic limit (HEL) is included, and (3) phase change effects are considered. Experimental data for alumina

ceramics reported in the literature [82, 95–100] indicated that the material strength softening formulation in the JHB model is more representative of experiments when compared to the JH1 and JH2 models by demonstrating a linear response at low pressures, nonlinear response at higher pressures up to HEL, and pressure and strain-rate independent response when the pressure level drove the material over the its HEL (see Figure 1(b)). All these improvements over the previous JH models are important when modelling shock and impact conditions, as we do in this study. A brief summary of the JHB model is presented below, and a detailed explanation of parameterization is described later in Section 3. The associated parameters and units of the JHB model are shown in Table 1, and this will be revisited later.

*JHB strength model

In the JHB model, the material strength is dependent on hydrostatic pressure, equivalent strain rate, and the accumulation of damage in the material. In the JHB strength model, the strength of the material is represented by a linear curve up to a pressure value of P_1 (intact strength constant), where the corresponding strength is σ_1. Prior to P_1, the equivalent material strength is $\sigma = 0$ at $P = 0$. After the P_1, the intact strength of the material is expressed in von Mises equivalent stress as [20]:

$$\sigma_{eq,i} = \sigma_1 + (\sigma_{max} - \sigma_1)\left[1 - e^{-\alpha_1(p-p_1)}\right] \tag{1}$$

$$\alpha_1 = \frac{\sigma_1}{(\sigma_{max} - \sigma_1)(P_1 + T)} \tag{2}$$

where σ_{max} is the maximum intact strength of the material (i.e., compressive) and T is the hydrostatic tensile strength. Similarly, the strength of the failed material (when D=1) is expressed as [20]:

$$\sigma_{eq,f} = \sigma_2 + \left(\sigma^{maxf} - \sigma_2\right)\left[1 - e^{-\alpha_2(p-p_2)}\right] \tag{3}$$

$$\alpha_2 = \frac{\sigma_1}{P_2(\sigma^{maxf} - \sigma_2)} \tag{4}$$

Considering the strain rate effect on strength, the strength of the material is expressed as [20]:

$$\sigma_{eq} = \sigma_{eq,0}[1 + \widetilde{c} ln\left(\frac{\dot{\varepsilon}}{\dot{\varepsilon}_0}\right)] \tag{5}$$

where $\widetilde{c}$ is the strain rate effect coefficient, $\dot{\varepsilon}$ is the equivalent strain rate, and $\dot{\varepsilon}_0 = 1\ s^{-1}$ is the reference strain rate.

* JHB damage model

The accumulation of damage in the material is represented by a form that is similar to the Johnson-Cook fracture model [20]:

$$D = \sum \Delta\varepsilon^p / \varepsilon_f^p \tag{6}$$

where $\Delta\varepsilon^p$ is the incremental equivalent plastic strain during a computational cycle, and $\varepsilon_f^p = f(p)$ is the plastic strain at fracture and is defined as [20]:

$$\varepsilon_f^p = D_1\left(P^* + T^*\right)^n \tag{7}$$

where both D_1 and n are material constants. P^* is the dimensionless pressure and $P^* = P/\sigma_{max}$. T^* is the dimensionless hydrostatic pressure and $T^* = T/\sigma_{max}$. The

ε_f^p increases as P^* increases, and the material does not undergo any plastic strain at $P^* = -T^*$.

*JHB pressure-volume relationship with bulking

It is worth noting that the phase change effect of alumina ceramic is not considered in this work given the lack of proof in the literature of such phenomenon in alumina [45] (see Section 3 for details). Without considering the phase change effect, the hydrostatic pressure begins to accumulate before failure and is defined as [20]:

$$P = k_1\mu + k_2\mu^2 + k_3\mu^3 \tag{8}$$

$$\mu = \frac{\rho}{\rho_0} - 1 \tag{9}$$

where k_1 (bulk modulus), k_2, and k_3 are material constants. ρ and ρ_0 is the current density and reference density, respectively. For tensile stress states ($\mu < 0$), Equation (8) is replaced by $P = k_1\mu$.

The model [20] also considers the bulking effect when the material fails ($D = 1$) [20]. The effect of bulking results in an increase in the pressure and volume [101]. The bulking effect is represented by having an incremental pressure ΔP adding to Equation (8) [20]:

$$P = k_1\mu + k_2\mu^2 + k_3\mu^3 + \Delta P \tag{10}$$

The bulking-induced pressure increment is determined from energy considerations. When the material fails, the material strength decreases, and this corresponds to a decrease in the deviatoric stresses, further resulting in a decrease in the incremental internal elastic energy. The loss of incremental internal elastic energy is converted to potential hydrostatic energy by incrementally increasing ΔP. The general expression for the elastic internal energy is [20]:

$$U = \frac{\sigma^2}{6G} \tag{11}$$

where G is the shear modulus of elasticity.

The incremental energy loss is computed as [20]:

$$\Delta U = U_i - U_f \tag{12}$$

where U_i is the internal energy of the intact material before failure and U_f is the internal energy of the material when it is failed. The conversion between the pressure and elastic internal energy is [20]:

$$\Delta P\mu_f + \Delta P^2/\left(2k_1\right) = \beta\Delta U \tag{13}$$

where μ_f is the value of μ when the material is failed, and β is the fraction ($0 \leq \beta \leq 1$) of the internal (deviator) energy loss converted to potential hydrostatic energy. The first term $\left(\Delta P\mu_f\right)$ is the approximate potential energy for $\mu > 0$, and the second term $\left(\Delta P^2/\left(2k_1\right)\right)$ is the corresponding potential energy for $\mu < 0$. The ΔP is given by [20]:

$$\Delta P = -k_1\mu_f + \sqrt{\left(k_1\mu_f\right)^2 + 2\beta k_1\Delta U} \tag{14}$$

The bulking pressure is computed only for failure under compression $\left(\mu_f > 0\right)$. Note that $\Delta P = 0$ for $\beta = 0$ and that ΔP increases as ΔU increases and/or μ_f decreases.

Johnson-Cook material model for tungsten alloy projectile

In this study, the Johnson-Cook (JC) plasticity model is selected to define the material behavior of the tungsten alloy projectile [42] (see Figure 3), and the corresponding material constants are provided in Table 5. The JC model reasonably captures the material response when subjected to high strain rate loading [42, 47]. In addition, the JC model is commonly used in ballistic impact simulations due to its uncoupled approach in calibrating material parameters [17, 102]. In this section, a brief summary of the model is provided. *Johnson-Cook strength model The flow stress-equivalent plastic strain relation of the JC model is given as [17]:

$$\sigma_y = (A + B(\varepsilon^p)^n)(1 + C \ln \dot{\varepsilon}_p^*)(1 - \ {T_{JC}}^m) \tag{15}$$

where σ_y is the yield stress, ε^p is the equivalent plastic strain, $\dot{\varepsilon}_p$ is the equivalent plastic strain rate, and A, B, and C are the material constants. The $\dot{\varepsilon}_p^*$ and T_{JC} are obtained from:

$$\dot{\varepsilon}_p^* = \frac{\dot{\varepsilon}_p}{\dot{\varepsilon}_0} \tag{16}$$

$$T_{JC} = \frac{T - T_0}{T_{melt} - T_0} \tag{17}$$

where $\dot{\varepsilon}_0$ is the reference strain rate, T is the current temperature, T_{melt} is the melting temperature, and T_0 is the reference temperature.

Multi-layer perceptron neural networks

The multilayer perceptron (MLP) approach is a useful tool in solving non-linear classification and regression problems [103], and it has been employed in this work to develop statistical models for impact performance optimization. The MLPs in this study are trained using forward and backward propagation algorithms. In the forward algorithm, a linear activation function is used to map the weighted inputs to the output of each neuron, and each layer in the MLP is described mathematically as [104, 105]:

$$a_i^{(l)} = f\left(\sum_{j=1}^{n} a_i^{(l)} \theta_{ij}^{(l)} + \theta_{0,j}^{(l)}\right), 1 \leq l \leq L \tag{18}$$

where the $a_i^{(l)}$ is the activation of the $ı^{th}$ neuron in the l^{th} layer, $\theta_{ij}^{(l)}$ represents the weight that is used to send the input to the i^{th} neuron, from the j^{th} neuron in layer l, and $\theta_{0,j}^{(l)}$ represents the bias in l^{th} layer.

The Relu function is chosen for nonlinear activation for this work, which is described as [104, 105]:

$$f(x) = \max(0, x) \tag{19}$$

For the back-propagation training, all the weights and thresholds are updated using the root mean squared propagation (RMS-prop) algorithm [104, 105]:

$$\theta_i := \theta_i + \Delta\theta_i \tag{20}$$

$$\Delta\theta_i = -\eta \frac{\partial J(\theta)}{\partial \theta_i} \tag{21}$$

where η is the learning rate factor, and $\frac{\partial J(\theta)}{\partial \theta_i}$ is the partial derivatives of the cost function with respect to weights. The partial derivatives of the cost function with respect to all of the parameters that feed into the current layer and the output layer $\delta(L-1)$ are computed as [104, 105]:

$$\frac{\partial J(\theta)}{\partial \theta_{ij}^{(l)}} = \left(\delta^{(l+1)}\right)^T a^{(l)} \tag{22}$$

$$\frac{\partial J(\theta)}{\partial \theta_{ij}^{(L-1)}} = \left(\delta^{(L)}\right)^T a^{(L-1)} \tag{23}$$

The error term δ for the output layer and the hidden layers are computed as [104, 105]:

$$\delta^{(L)} = \frac{1}{m}\left(y - a^{(L)}\right) f'\left(a^{(L)}\right) \tag{24}$$

$$\delta_j^{(l)} = f'\left(a^{(l)}\right) \sum_{i=1}^{n} \delta_i^{(l+1)} \theta_{ij}^{(l)} \tag{25}$$

Finally, the overall performance of the MLP is measured by the mean squared error (MSE) which is expressed by [104, 105]:

$$J(\theta) = \frac{1}{2m^*} \sum_{i=1}^{m^*} \left(h_\theta\left(x^{(i)}\right) - y^{(i)}\right)^2 \tag{26}$$

where m^* is the number of training samples, $h_\theta(x^{(i)})$ is the vector of predicted values based on the training samples, and $y^{(i)}$ labels the vector of actual values.

Table 5: Johnson-Cook material constants of the tungsten alloy long rod projectile that is taken from Bresciani et al. [42].

Model Parameters	Notation	Value
Density (kg/m^3)	ρ_p	17600
Shear modulus (GPa)	G_p	152
Elastic modulus (GPa)	E_p	314
Quasi-static tensile yield strength (GPa)	A	1.6
Hardening exponent (GPa)	B_p	0.1765
Thermal softening exponent	C_p	0.016
Strain rate sensitivity coefficient	N	0.12
Temperature exponent	M	1
Melting temperature (K)	T_{melt}	3695
Room temperature (K)	T_0	291
Heat capacity (J/Kg*K)	c_p	384
Damage Parameters		
Damage coefficient 1	D_1^*	0
Damage coefficient 2	D_2^*	1
Damage coefficient 3	D_3^*	-1.5
Damage coefficient 4	D_4^*	0.042
Damage coefficient 5	D_5^*	0
Equation of State Parameters		
Gruneisen coefficient	G_2	1.67
Linear Hugoniot slope coefficient	S_1	1.237
Bulk speed of sound (m/s)	C_1	4030

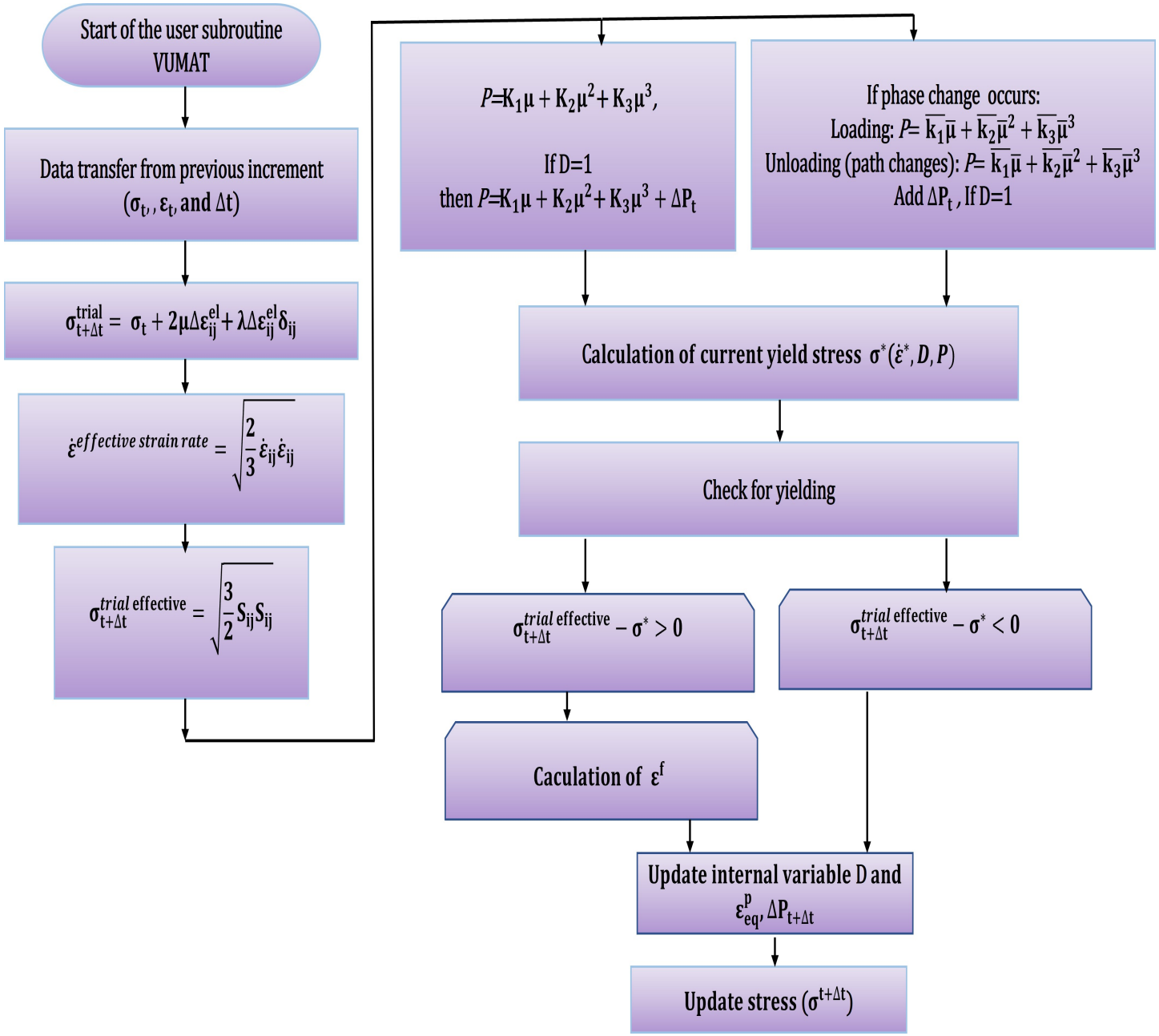

Figure 13: The flowchart for writing the subroutine code of the JHB material model in LS-DYNA.

Appendix B: Results

Single element verification

The JHB material model has been implemented into the finite element code of LS-DYNA through a user-defined subroutine. To demonstrate the accuracy of the code, a single-element model has been developed and utilized to verify the implementation of the JHB material model in LS-DYNA following the approach outlined by Johnson et al. [20], where the loading history of the element interrogates high deviatoric and hydrostatic pressures in this verification. The material constants used in the single element simulations are based on the material constants provided in the original paper by Johnson et al. [20] for aluminum nitride. The material constants for the alumina studied here are validated in Section 3 for plate and ballistic impact cases that exhibit the high strain rate and high-pressure behavior. The single-element model is established in LS-DYNA with the dimension of 1 m $\times$ 1 m $\times$ 1 m, as shown in Figure 14 (a). The confined boundary conditions are employed to constrain the element to displace at four sides and bottom (fixed), and thus, the element is only allowed to displace vertically along the z-direction. Next, the element is subjected to external load via displacement control on the top surface. For each simulation, the element is compressed to a strain of nearly 14%, then unloaded to allow recovery to its initial length. The verification of the subroutine codes is achieved by comparing the equivalent stress-pressure curve provided in Johnson et al. [20]. Figure 14 (b) shows the equivalent stress vs. pressure plot of the single element under loading and unloading conditions in comparison with the response reported in Johnson et al. [20]. The main critical stages of the material under compressive loading followed by tensile loading are identified on the plot with inserted numbers (Figure 14 (b)): (1-3) the material undergoes elastic deformation up to yielding followed by plastic deformation with damage accumulation; (3-4) the material failure lead to an abrupt increase in the pressure due to bulking, where the bulking phenomenon as a consequence of the decrease in axial stress due to the decrease in the deviatoric stress (i.e., degradation in material strength); and (4-8) the material undergoes phase transformation and reversal of loading. Overall, it is observed that the resultant curves generated from the implemented code in this work is in reasonable agreement with the one reported in the literature [20], as demonstrated in Figure 14(b), with slight deviations occurring at the end of the first and third stages. These deviations are likely caused by the differences in software and numerical algorithms between the studies.

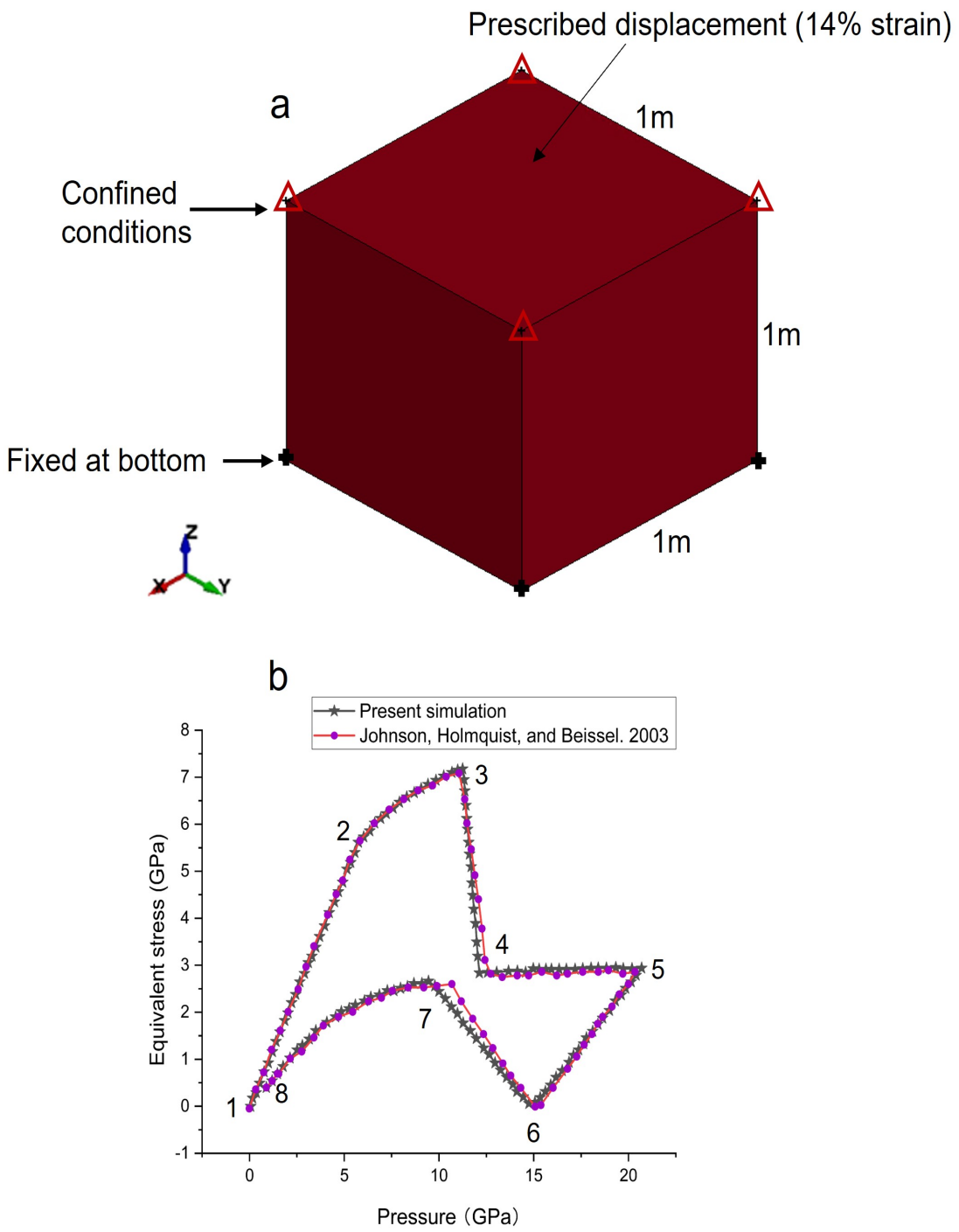

Figure 14: Verification of the implemented user-defined sub-routine of the Johnson-Holmquist-Beissel model through a single element simulation under uniaxial loading-unloading condition, where the element is constrained from displacing of sides and bottom with an external prescribed displacement acts on the top surface. (a) Single element model configuration.(b) Predicted equivalent stress vs. pressure plot compared to the numerical result published by Johnson et al. [20].

Figure 15 shows the damage evolution images for both the alumina ceramic tile and the projectile under ballistic impact velocity of 901 m/s. In Figure 15, the conical damages starts to form on the front surface of the ceramic as it is impacted by projectile at 8 µs. Next, the fractured cone starts to develop in the ceramic from the contact surface and propagates towards the back surface between 8 µs and 30 µs, and the completed

perforation and erosion of projectile is observed at 72 µs.

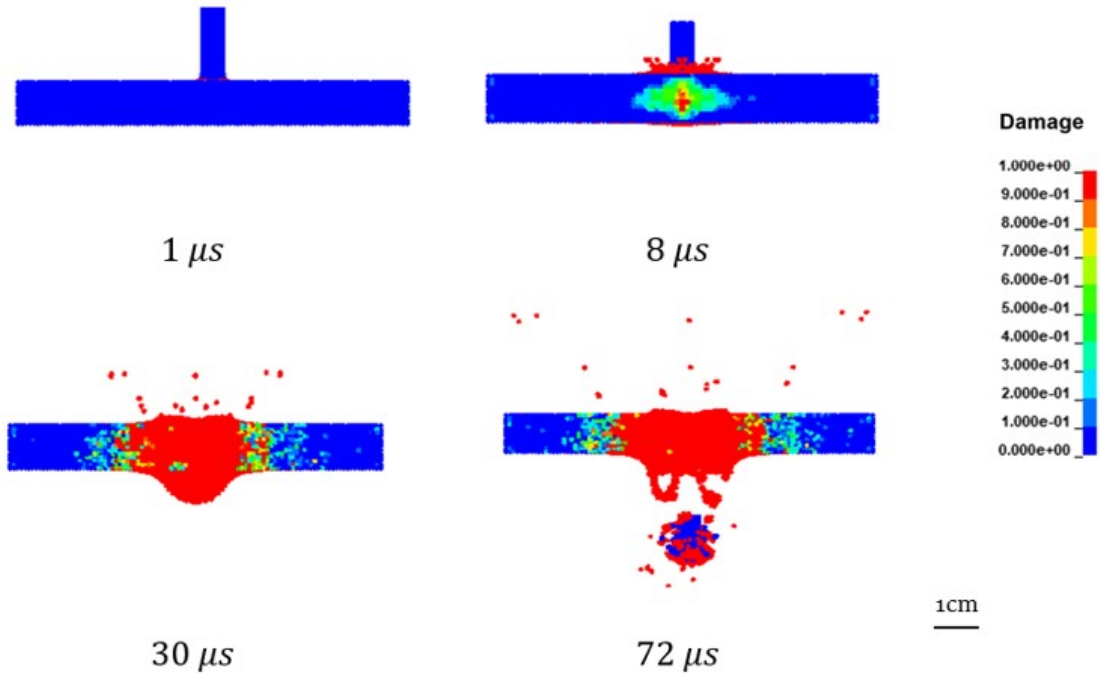

Figure 15: Damage evolution in alumina ceramic tile undergoing penetration of tungsten long rod projectile at time of 1 µs, 8 µs, 30 µs, and 72 µs under ballistic impact.

References

[1] D. Luo, Y. Wang, F. Wang, H. Cheng, B. Zhang, Y. Zhu, The influence of metal cover plates on ballistic performance of silicon carbide subjected to large-scale tungsten projectile, Materials & Design 191 (2020) 108659.

[2] S. Walley, Historical review of high strain rate and shock properties of ceramics relevant to their application in armour, Advances in Applied Ceramics 109 (8) (2010) 446–466.

[3] Y. Wade-Zhu, J. Wade-Zhu, H. Wu, J. Binner, B. Vaidhyanathan, The ballistic impact performance of nanocrystalline zirconia-toughened alumina (nzta) and alumina ceramics, Journal of the European Ceramic Society 41 (2) (2021) 1427–1437.

[4] S. Savio, V. Madhu, Ballistic performance evaluation of ceramic tiles with respect to projectile velocity against hard steel projectile using dop test, International Journal of Impact Engineering 113 (2018) 161–167.

[5] M. Silva, D. Stainer, H. Al-Qureshi, O. Montedo, D. Hotza, Alumina-based ceramics for armor application: mechanical characterization and ballistic testing, Journal of Ceramics 2014 (2014).

[6] D. Hu, Y. Zhang, Z. Shen, Q. Cai, Investigation on the ballistic behavior of mosaic sic/uhmwpe composite armor systems, Ceramics International 43 (13) (2017) 10368–10376.

[7] B. Tepeduzu, R. Karakuzu, Ballistic performance of ceramic/composite structures, Ceramics International 45 (2) (2019) 1651–1660.

[8] J. D. Hogan, L. Farbaniec, D. Mallick, V. Domnich, K. Kuwelkar, T. Sano, J. W. McCauley, K. T. Ramesh, Fragmentation of an advanced ceramic under ballistic impact: mechanisms and microstructure, International journal of impact engineering 102 (2017) 47–54.

[9] D. Mallick, M. Zhao, J. Parker, V. Kannan, B. Bosworth, D. Sagapuram, M. Foster, K. Ramesh, Laser-driven flyers and nanosecond-resolved velocimetry for spall studies in thin metal foils, Experimental Mechanics 59 (5) (2019) 611–628.

[10] R. Scazzosi, M. Giglio, A. Manes, Fe coupled to sph numerical model for the simulation of high-velocity impact on ceramic based ballistic shields, Ceramics International 46 (15) (2020) 23760–23772.

[11] E. Strassburger, S. Bauer, S. Weber, H. Gedon, Flash x-ray cinematography analysis of dwell and penetration of small caliber projectiles with three types of sic ceramics, def. technol. 12 (2016) 277–283.

[12] X. Zhang, A. Serjouei, I. Sridhar, Criterion for interface defeat to penetration transition of long rod projectile impact on ceramic armor, Thin-Walled Structures 126 (2018) 266–284.

[13] A. R. Yazdani, Investigation on high-velocity impact performance of multi-layered alumina ceramic armors with polymeric interlayers, Journal of Composite Materials 50 (2015) 3561–3576.

[14] M. N. C. X.Quan, R.A.Clegg, Numerical simulation of long rods impacting silicon carbide targets using jh-1 model, International Journal of Impact Engineering 33 (2006) 634–644.

[15] S. Chakraborty, M. R. I. Islam, A. Shaw, L. Ramachandra, S. Reid, A computational framework for modelling impact induced damage in ceramic and ceramic-metal composite structures, Composite Structures 164 (2017) 263–276.

[16] K. Z.Fawaz, W. Zheng, Numerical simulation of normal and oblique ballistic impact on ceramic composite armours, Composite Structures 63 (2004) 387–395.

[17] G. Toussaint, I. Polyzois, Steel spheres impact on alumina ceramic tiles: Experiments and finite element simulations, International Journal of Applied Ceramic Technology 16 (6) (2019) 2131–2152.

[18] G. Johnson, T. Holmquist, A computational constitutive model for brittle materials subjected to large strains, high strain rates and high pressures, Shock wave and high-strain-rate phenomena in materials (1992) 1075–1081.

[19] G. R. Johnson, T. J. Holmquist, An improved computational constitutive model for brittle materials, in: AIP conference proceedings, Vol. 309, American Institute of Physics, 1994, pp. 981–984.

[20] G. R. Johnson, T. J. Holmquist, S. R. Beissel, Response of aluminum nitride (including a phase change) to large strains, high strain rates, and high pressures, Journal of Applied Physics 94 (3) (2003) 1639–1646.

[21] M. R. I. Islam, J. Zheng, R. C. Batra, Ballistic performance of ceramic and ceramic-metal composite plates with jh1, jh2 and jhb material models, International Journal of Impact Engineering 137 (2020) 103469.

[22] D. Grady, R. Moody, Shock compression profiles in ceramics, Tech. rep., Sandia National Lab.(SNL-NM), Albuquerque, NM (United States) (1996).

[23] F. Cui, G. Wu, M. Tian, W. Li, Effect of ceramic properties and depth-of-penetration test parameters on the ballistic performance of armour ceramics, Defence Science Journal 67 (3) (2017) 260.

[24] Y. Xiao, H. Wu, X. Ping, On the simulation of fragmentation during the process of ceramic tile impacted by blunt projectile with sph method in ls-dyna, Computer Modeling in Engineering & Sciences 122 (3) (2020) 923–954.

[25] R. Yao, F. Su, R. Mao, Influence of interfacial bonding conditions on the anti-penetration performance of ceramic/metal composite targets, International Journal of Mechanics and Materials in Design 15 (4) (2019) 833–844.

[26] M. Liu, G. Liu, Smoothed particle hydrodynamics (sph): an overview and recent developments, Archives of computational methods in engineering 17 (1) (2010) 25–76.

[27] S. Chakraborty, A. Shaw, A pseudo-spring based fracture model for sph simulation of impact dynamics, International Journal of Impact Engineering 58 (2013) 84–95.

[28] S. Gharehdash, M. Barzegar, I. B. Palymskiy, P. A. Fomin, Blast induced fracture modelling using smoothed particle hydrodynamics, International Journal of Impact Engineering 135 (2020) 103235.

[29] F. Ren, T. Fang, X. Cheng, Study on rock damage and failure depth under particle water-jet coupling impact, International Journal of Impact Engineering 139 (2020) 103504.

[30] H. Ai, T. Ahrens, Simulation of dynamic response of granite: A numerical approach of shock-induced damage beneath impact craters, International Journal of Impact Engineering 33 (1-12) (2006) 1–10.

[31] D. Somasundaram, S. Roy, M. Trabia, B. O'TOOLE, R. HIXSON, Parametric sensitivity comparison of simulation models for flyer plate impact experiments, International Journal of Computational Methods and Experimental Measurements 3 (4) (2015) 305–315.

[32] M. K. Almustafa, M. L. Nehdi, Machine learning model for predicting structural response of rc columns subjected to blast loading, International Journal of Impact Engineering 162 (2022) 104145.

[33] S. Ryan, S. Thaler, Artificial neural networks for characterising whipple shield performance, International Journal of Impact Engineering 56 (2013) 61–70.

[34] Z. Liu, C. Wu, M. Koishi, A deep material network for multiscale topology learning and accelerated nonlinear modeling of heterogeneous materials, Computer Methods in Applied Mechanics and Engineering 345 (2019) 1138–1168.

[35] L. Luo, B. Zhang, G. Zhang, Y. Xu, Rapid prediction of cured shape types of composite laminates using a fem-ann method, Composite Structures 238 (2020) 111980.

[36] Y. Zhang, D. W. Apley, W. Chen, Bayesian optimization for materials design with mixed quantitative and qualitative variables, Scientific reports 10 (1) (2020) 1–13.

[37] Z. Yang, Y. C. Yabansu, R. Al-Bahrani, W.-k. Liao, A. N. Choudhary, S. R. Kalidindi, A. Agrawal, Deep learning approaches for mining structure-property linkages in high contrast composites from simulation datasets, Computational Materials Science 151 (2018) 278–287.

[38] Y. Gao, D. Li, W. Zhang, Z. Guo, C. Yi, Y. Deng, Constitutive modelling of the tib2–b4c composite by experiments, simulation and neutral network, International Journal of Impact Engineering 132 (2019) 103310.

[39] R. Bobbili, B. Ramakrishna, V. Madhu, An artificial intelligence model for ballistic performance of thin plates, Mechanics Based Design of Structures and Machines (2020) 1–12.

[40] L. S. Liu, Q. J. Zhang, P. C. Zhai, The optimization design on metal/ceramic fgm armor with neural net and conjugate gradient method, in: Materials Science Forum, Vol. 423, Trans Tech Publ, 2003, pp. 791–796.

[41] S. Nemat-Nasser, S. Sarva, J. B. Isaacs, D. W. Lischer, Novel ideas in multifunctional ceramic armor design, Ceramic transactions 134 (2002) 511–526.

[42] L. M. Bresciani, A. Manes, T. Romano, P. Iavarone, M. Giglio, Numerical modelling to reproduce fragmentation of a tungsten heavy alloy projectile impacting a ceramic tile: Adaptive solid mesh to the sph technique and the cohesive law, International Journal of Impact Engineering 87 (2016) 3–13.

[43] A. Tasdemirci, G. Tunusoglu, M. Güden, The effect of the interlayer on the ballistic performance of ceramic/composite armors: Experimental and numerical study, International Journal of Impact Engineering 44 (2012) 1–9.

[44] S. Choudhary, P. K. Singh, S. Khare, K. Kumar, P. Mahajan, R. K. Verma, Ballistic impact behaviour of newly developed armour grade steel: an experimental and numerical study, International Journal of Impact Engineering 140 (2020) 103557.

[45] C. S. Alexander, W. D. Reinhart, T. F. Thornhill, L. C. Chhabildas, Armor options: A comparison of the dynamic response of materials in the aluminum oxide–aluminum nitride family, International Journal of Applied Ceramic Technology 7 (5) (2010) 587–594.

[46] S. Bavdekar, G. Subhash, Comparison of pressure-sensitive strength models for ceramics under ultrahigh confinement, International Journal of Impact Engineering 118 (2018) 60–66.

[47] E. Simons, J. Weerheijm, L. J. Sluys, Simulating brittle and ductile response of alumina ceramics under dynamic loading, Engineering Fracture Mechanics 216 (2019) 106481.

[48] R. Krashanitsa, An inverse computational approach for the identification of the parameters of the constitutive model for damaged ceramics subjected to impact loading, The University of Arizona, 2005.

[49] D. S. Cronin, K. Bui, C. Kaufmann, G. McIntosh, T. Berstad, D. Cronin, Implementation and validation of the johnson-holmquist ceramic material model in ls-dyna, in: 4th European LS-dyna users conference, Vol. 1, 2003, pp. 47–60.

[50] R. Vignjevic, N. Djordjevic, T. De Vuyst, S. Gemkow, Modelling of strain softening materials based on equivalent damage force, Computer Methods in Applied Mechanics and Engineering 335 (2018) 52–68.

[51] R. Vignjevic, N. Djordjevic, S. Gemkow, T. De Vuyst, J. Campbell, Sph as a nonlocal regularisation method: Solution for instabilities due to strain-softening, Computer Methods in Applied Mechanics and Engineering 277 (2014) 281–304.

[52] W. Reinhart, L. Chhabildas, Strength properties of coors ad995 alumina in the shocked state, International journal of impact engineering 29 (1-10) (2003) 601–619.

[53] J. W. Swegle, D. L. Hicks, S. Attaway, Smoothed particle hydrodynamics stability analysis, Journal of computational physics 116 (1) (1995) 123–134.

[54] D. A. Shockey, A. Marchand, S. Skaggs, G. Cort, M. Burkett, R. Parker, Failure phenomenology of confined ceramic targets and impacting rods, Ceramic transactions 134 (2002) 385–402.

[55] D. Curran, L. Seaman, T. Cooper, D. Shockey, Micromechanical model for comminution and granular flow of brittle material under high strain rate application to penetration of ceramic targets, International Journal of Impact Engineering 13 (1) (1993) 53–83.

[56] A. Krell, E. Strassburger, Order of influences on the ballistic resistance of armor ceramics and single crystals, Materials Science and Engineering: A 597 (2014) 422–430.

[57] Z. Rozenberg, Y. Yeshurun, The relation between ballastic efficiency and compressive strength of ceramic tiles, International journal of impact engineering 7 (3) (1988) 357–362.

[58] G. Kleiser, L. Chhabildas, W. Reinhart, Comparison of dynamic compression behavior of single crystal sapphire to polycrystalline alumina, International journal of impact engineering 38 (6) (2011) 473–479.

[59] T. Mashimo, M. Uchino, A. Nakamura, T. Kobayashi, E. Takasawa, T. Sekine, Y. Noguchi, H. Hikosaka, K. Fukuoka, Y. Syono, Yield properties, phase transition, and equation of state of aluminum nitride (aln) under shock compression up to 150 gpa, Journal of Applied Physics 86 (12) (1999) 6710–6716.

[60] S. Sukanta Chakraborty, L.S.Ramachandra, A computational framework for modelling impact induced damage in ceramic and ceramic-metal composite structures, Composite Structures 164 (2017) 263–276.

[61] G. Subhash, A. Awasthi, D. Ghosh, Dynamic Response of Advanced Ceramics, John Wiley & Sons, 2021.

[62] W. Li, K. Ramesh, A finite deformation framework for mechanism-based constitutive models of the dynamic behavior of brittle materials, Journal of the Mechanics and Physics of Solids 155 (2021) 104518.

[63] D. Grady, Shock-wave compression of brittle solids, Mechanics of Materials 29 (3-4) (1998) 181–203.

[64] Y. Zhu, G. Liu, Y. Wen, C. Xu, W. Niu, G. Wang, Back-spalling process of an al2o3 ceramic plate subjected to an impact of steel ball, International Journal of Impact Engineering 122 (2018) 451–471.

[65] H. Purwanto, M. Dzulfikar, M. Tauviqirrahman, I. Syafaat, M. Arifin, Residual velocity and kinetic energy of the ballistic simulations test on hardened medium carbon steel plate, in: Journal of Physics: Conference Series, Vol. 1517, IOP Publishing, 2020, p. 012003.

[66] A. B. Dresch, J. Venturini, S. Arcaro, O. R. Montedo, C. P. Bergmann, Ballistic ceramics and analysis of their mechanical properties for armour applications: A review, Ceramics International 47 (7) (2021) 8743–8761.

[67] M. Parsazadeh, G. Fisher, A. McDonald, J. D. Hogan, Computational modelling of the effect of microstructure on the abrasive wear resistance of tungsten-carbide nickel composite coatings under sub-critical cyclic impact loading, Ceramics International (2022).

[68] P. Karandikar, G. Evans, S. Wong, M. Aghajanian, M. Sennett, A review of ceramics for armor applications, Advances in Ceramic Armor IV 29 (2009) 163–175.

[69] C. Kaufmann, D. Cronin, M. Worswick, G. Pageau, A. Beth, Influence of material properties on the ballistic performance of ceramics for personal body armour, Shock and Vibration 10 (1) (2003) 51–58.

[70] F. de Oliveira Braga, F. S. da Luz, S. N. Monteiro, É. P. Lima Jr, Effect of the impact geometry in the ballistic trauma absorption of a ceramic multilayered armor system, Journal of materials research and technology 7 (4) (2018) 554–560.

[71] C. J. Yungwirth, D. D. Radford, M. Aronson, H. N. Wadley, Experiment assessment of the ballistic response of composite pyramidal lattice truss structures, Composites Part B: Engineering 39 (3) (2008) 556–569.

[72] S. McKown, Y. Shen, W. Brookes, C. Sutcliffe, W. Cantwell, G. Langdon, G. Nurick, M. Theobald, The quasi-static and blast loading response of lattice structures, International Journal of Impact Engineering 35 (8) (2008) 795–810.

[73] M. A. Iqbal, G. Gupta, A. Diwakar, N. Gupta, Effect of projectile nose shape on the ballistic resistance of ductile targets, European Journal of Mechanics-A/Solids 29 (4) (2010) 683–694.

[74] P. Sathananthan, A. Sirois, D. Singh, D. Cronin, Sphere on tile ballistic impact experiment to characterize the response of soda lime glass, International Journal of Impact Engineering 133 (2019) 103321.

[75] E. Haney, G. Subhash, Damage mechanisms perspective on superior ballistic performance of spinel over sapphire, Experimental Mechanics 53 (1) (2013) 31–46.

[76] H. An, Y. Song, H. Liu, H. Han, Combined finite-discrete element modelling of dynamic rock fracture and fragmentation during mining production process by blast, Shock and Vibration 2021 (2021).

[77] K. Ramesh, L. Graham-Brady, W. A. Goddard, R. C. Hurley, M. Robbins, A. L. Tonge, A. Bhattacharjee, J. T. Clemmer, Q. Zeng, W. Li, et al., Models for the behavior of boron carbide in extreme dynamic environments, Journal of the American Ceramic Society 105 (5) (2022) 3043–3061.

[78] K. KMW, Ceramic materials for light-weight ceramic polymer armor systems.

[79] K. Eckle, J. Schmidt-Hieber, A comparison of deep networks with relu activation function and linear spline-type methods, Neural Networks 110 (2019) 232–242.

[80] S. Ruder, An overview of gradient descent optimization algorithms, arXiv preprint arXiv:1609.04747 (2016).

[81] S. Sayahlatifi, C. Shao, A. McDonald, J. Hogan, 3d microstructure-based finite element simulation of cold-sprayed al-al2o3 composite coatings under quasi-static compression and indentation loading, Journal of Thermal Spray Technology (2021) 1–17.

[82] M. Shafiq, G. Subhash, An extended mohr–coulomb model for fracture strength of intact brittle materials under ultrahigh pressures, Journal of the American Ceramic Society 99 (2) (2016) 627–630.

[83] A. Lamberts, M. Geers, J. van Dommelen, H. de Lange, A. Huizinga, P. BV, Numerical simulation of ballistic impacts on ceramic material, Nederland: Eindhoven University of Technology (2007).

[84] D. Fernández-Fdz, R. Zaera, A new tool based on artificial neural networks for the design of lightweight ceramic–metal armour against high-velocity impact of solids, International Journal of Solids and Structures 45 (25-26) (2008) 6369–6383.

[85] V. Bushaev, Understanding rmsprop-faster neural network learning, Towards Data Science (2018).

[86] Y. Bengio, Practical recommendations for gradient-based training of deep architectures, in: Neural networks: Tricks of the trade, Springer, 2012, pp. 437–478.

[87] D. Masters, C. Luschi, Revisiting small batch training for deep neural networks, arXiv preprint arXiv:1804.07612 (2018).

[88] M. Wilkins, C. Cline, C. Honodel, Fourth progress report of light armor program., Tech. rep., California Univ., Livermore. Lawrence Radiation Lab. (1969).

[89] D. B. Rahbek, B. B. Johnsen, Fragmentation of an armour piercing projectile after impact on composite covered alumina tiles, International Journal of Impact Engineering 133 (2019) 103332.

[90] D. B. Rahbek, J. W. Simons, B. B. Johnsen, T. Kobayashi, D. A. Shockey, Effect of composite covering on ballistic fracture damage development in ceramic plates, International Journal of Impact Engineering 99 (2017) 58–68.

[91] L. Wu, D. Huang, F. Bobaru, A reformulated rate-dependent visco-elastic model for dynamic deformation and fracture of pmma with peridynamics, International Journal of Impact Engineering 149 (2021) 103791.

[92] R. Browning, K. Danielson, M. Adley, Higher-order finite elements for lumped-mass explicit modeling of high-speed impacts, International Journal of Impact Engineering 137 (2020) 103458.

[93] M. Anghileri, L.-M. Castelletti, F. Invernizzi, M. Mascheroni, A survey of numerical models for hail impact analysis using explicit finite element codes, International Journal of Impact Engineering 31 (8) (2005) 929–944.

[94] J. O. Hallquist, et al., Ls-dyna keyword user's manual, Livermore Software Technology Corporation 970 (2007) 299–800.

[95] H. Heard, C. Cline, Mechanical behaviour of polycrystalline beo, al2o3 and aln at high pressure, Journal of Materials Science 15 (8) (1980) 1889–1897.

[96] Z. Rosenberg, D. Yaziv, Y. Yeshurun, S. Bless, Shear strength of shock-loaded alumina as determined with longitudinal and transverse manganin gauges, Journal of applied physics 62 (3) (1987) 1120–1122.

[97] W. Chen, G. Ravichandran, Failure mode transition in ceramics under dynamic multiaxial compression, International Journal of Fracture 101 (1) (2000) 141–159.

[98] Z. Rosenberg, N. Brar, S. Bless, Dynamic high-pressure properties of aln ceramic as determined by flyer plate impact, Journal of applied physics 70 (1) (1991) 167–171.

[99] M. Normandia, Impact response and analysis of several silicon carbides, International Journal of Applied Ceramic Technology 1 (3) (2004) 226–234.

[100] S. Chocron, C. E. Anderson Jr, K. A. Dannemann, A. E. Nicholls, N. L. King, Intact and predamaged boron carbide strength under moderate confinement pressures, Journal of the American Ceramic Society 95 (1) (2012) 350–357.

[101] B. M. Koch, C. Lo, T. Sano, J. D. Hogan, Bulking as a mechanism in the failure of advanced ceramics, in: Hypervelocity Impact Symposium, Vol. 883556, American Society of Mechanical Engineers, 2019, p. V001T05A001.

[102] H. Farahani, M. Ketabchi, S. Zangeneh, Determination of johnson–cook plasticity model parameters for inconel718, Journal of Materials Engineering and Performance 26 (11) (2017) 5284–5293.

[103] M. W. Gardner, S. Dorling, Artificial neural networks (the multilayer perceptron)—a review of applications in the atmospheric sciences, Atmospheric environment 32 (14-15) (1998) 2627–2636.

[104] A. Ng, Machine learning, `https://www.coursera.org/learn/machine-learning#syllabus` (Jan. 2022).

[105] W. H. Delashmit, M. T. Manry, et al., Recent developments in multilayer perceptron neural networks, in: Proceedings of the seventh Annual Memphis Area Engineering and Science Conference, MAESC, 2005.